**ISAS - INTERNATIONAL SCHOOL FOR ADVANCED STUDIES**

# Radiative Processes in Compact Sources: a Study of Anisotropic Multiple Compton Scattering

*Thesis submitted for the degree of "Magister Philosophiæ"*

CANDIDATE

Francesco Haardt

SUPERVISOR

Prof. Aldo Treves

October 1993

**TRIESTE**

**SISSA - SCUOLA INTERNAZIONALE SUPERIORE DI STUDI AVANZATI**

TRIESTE

Strada Costiera 11

*all'amico Odorico, per averci salvato la vita...*

*"Su le coerte, giú le coerte"*

- Odorico Trevisan, October, 17th 1991 -

## ACKNOWLEDGEMENTS

Several people in different places and at different levels provided me with different kinds of support, moral, intellectual and, a bit more venial, financial.

My deep thanks are due to Aldo Treves, my supervisor at SISSA, for constant encouragment and stimulating discussions. I wish also to thank Dennis Sciama, always ready to help me in many ways whenever I need.

In Milano, I am delighted to thank Laura Maraschi, for putting me on my way to research, and teaching me how to display my thoughts in a intelligible fashion, and Gabriele Ghisellini, one of the most stimulating scientists and best friends I have ever known. Thank you GG! I would like to thank Chris Done for patiently struggling with my English and my laziness in running codes, and Giorgio Matt, a perfectly tuned collaborator, a fantastic cook, and another exiled A.C. Milan fan, surviving only thanks to Channel Four.

I thank the Astrophysical Sector of the University of Milano, the X-ray group in Leicester and the Observatory of Torino for hospitality.

Finally in these first two years of research, a lot of friends supported me with their love, in many cities, in different countries. The list would be a bit too long, so thanks! You know who you are.

I send my love to my parents, my brother and Barbara.

# Table of Contents

PREFACE 3

1. MOTIVATION

1.1 AGNs . . . . . 6

1.1.1 Observations and thermal models . . . . . 6

1.1.2 Problems for thermal models: a possible solution . . . . . 10

1.2 GBH: Cygnus X–1 . . . . . 15

References 18

Figure captions 23

2. THEORY

2.1 Basic equations . . . . . 26

2.2 Comptonization spectra . . . . . 28

2.2.1 General outline . . . . . 28

2.2.2 Iterative solution . . . . . 29

2.3 Energy and space evolution . . . . . 31

2.3.1 Isotropic kernel of single scattering . . . . . 31

2.3.2 Source volume integration . . . . . 33

2.4 Anisotropic IC emission . . . . . 35

2.4.1 Anisotropy coefficients . . . . . 35

2.4.2 Anisotropic first scattering distribution . . . . . 37

2.5 The thermal case . . . . . 40

2.5.1 Effective electron distribution . . . . . 40

2.5.2 Polynomial approximation . . . . . 41

2.5.3 Exemples of thermal IC spectra . . . . . 43

**References** 47

**Figure captions** 48

# Preface

Inverse Compton (IC) emission may play an important role in producing high energy photons in compact sources. Radiative models for radio quiet AGNs invoke such effect as the main X-ray and $\gamma$-ray production mechanism. In such models a low frequency radiation field (soft photon input) is Comptonized by hot electrons. The input photons are thermally emitted by nearby cold matter, possibly an accretion flow. In AGNs there is evidence that the accretion flow takes place in disk fashion. Hot electrons may form an active corona located above the surface of the disk. The presence of a corona surrounding an accretion disk is suggested also in Galactic X-ray binaries. In this kind of models, the source of soft photon is not homogeneously distributed within the scattering medium, so that the first scattering event is highly anisotropic. Many papers have been devoted to study Comptonization of low energy radiation in hot plasma Nevertheless only recently the importance of anisotropic inverse Compton process in AGNs has been emphasited. The total inverse Compton power emitted in different directions depends on direction itself, and this has important consequences for the fluorescent line emission observed in Seyfert galaxies and for the X-ray background model.

If one assume a non thermal distribution of ultrarelativistic electrons, the photon spectrum is essentially formed by a single scattering process, and the spectral shape is not affected by anisotropy. At different viewing angles the emitted spectrum shows the same power law shape, but with different luminosities. In thermal media the situation is different, since even for low optical depths the spectrum is shaped by multiple scatterings. Being essentially the anisotropic IC an effect at the first order of scattering, spectral distortions will be present in the low energy part of the Comptonized radiation

field.

In this thesis I studied the problem of Comptonization in AGNs and galactic sources, in a formal way. The thesis is divided into two distinct part: the first part deals with observations and *macrophysics*, i.e. models which have Comptonization as a main ingredient, while the second part is devoted to *microphysics*, i.e. a formal study of multiple Compton scattering.

In Part 1 I review the basic observations that indicate the importance of IC emission in Seyfert galaxies and black hole candidates. A brief description of a self consistent thermal model (Haardt & Maraschi 1991, 1993) is given. Possible problems of thermal plasmas in rapidly varying sources are outlined, and then I discuss a possible solution, namely a "quasi"–thermal model (Ghisellini, Haardt & Fabian 1993) that can account for the observed spectra.

In Part 2, the Boltzmann kinetik equation is solved iteratively for each scattering order distribution, in the approximation of isotropic scattering in the laboratory frame. This approximation is correct if the electrons have random orientated momenta, and if the photons do not show a preferntial direction. The spectral shape of the componized spectrum is obtained by means of the full relativistic kernel, allowing to deal with relativistic plasmas.

However, if the input photons are anisotropic, first scatterings should be treated in a different way. I developed an approximated method to write an anisotropic kernel, which is angle dependent with respect to an absolute reference system, e.g. the normal to a plane parallel slab. As an example the calculations are then carried out for a simple case, assuming Thomson scattering and neglecting the electron recoil. The analytical results are compared with Montecarlo simulations.

Part of the work of this thesis is based on the following published papers, while most of the Part 2 will appear in a paper in progress:

Ghisellini G., Haardt F., Fabian A. C., 1993, MNRAS, 263, L9

Haardt F., 1993, ApJ, 413, 680

Haardt F., Maraschi L., 1991, ApJ, 380, L51

Haardt F., Maraschi L., 1993, ApJ, 413, 507

Haardt F., Matt G., 1993, MNRAS, 261, 346

Haardt F., Done C., Matt G., Fabian A. C., 1993, ApJ, 411, L95

# Chapter 1

# Motivation

*The importance of Comptonization in Seyfert galaxies and black hole candidates is outlined. I briefly review recent observations which indicate multiple Inverse Compton scattering as the main source of the high energy emission from non-blazar AGN, and weakly magnetized X-ray binaries. The problems arising assuming a thermal electron distribution are discussed, and a possible soution is outlined.*

## 1.1 AGNs

### 1.1.1 Observation and Thermal Models

The origin of the X-ray emission from Seyfert galaxies and Quasars is still unknown. Successful models should satisfy three main observational constraints. The size of the X-ray production region must be small due to the fast variability, with typical time scales of hours (e.g. McHardy 1989). The observed spectrum in the medium X-ray range (2-20 keV) is close to a power law, with a small dispersion in the values of the spectral index, whose average for Seyfert galaxies is $\simeq 0.7 \pm 0.15$ (Mushotzky 1984, Turner & Pounds 1989). Whatever produces the X-rays is close to cold reflecting matter, as inferred from the presence of fluorescent Fe line emission and of a Compton reflection hump, which has a broad maximum around $\simeq$ 30 keV (Nandra 1991, Williams et al. 1992). In fact, after deconvolution of the latter component, the spectral index of the underlying

power law is revised to $\simeq 0.9$ (Pounds et al. 1990). Two classes of models have been proposed to explain the power law shape of the X-ray spectrum. One is based on the production of very high energy primaries and strong reprocessing via electromagnetic cascades leading to the formation of an $e^-e^+$ pair plasma (e.g. Zdziarski et al. 1990). The second involves multiple Compton scattering (Comptonization) of soft photons on a thermal population of hot electrons (e.g. Walter and Courvoisier 1992). In the first case the derived X-ray spectrum essentially depends only on the "compactness parameter", while in the second the temperature and optical depth of the scattering electrons are usually assigned in a rather "ad hoc" way.

Recently, the OSSE instrument on the Compton Gamma Ray Observatory has detected several Seyfert galaxies above 60 keV (Cameron et al. 1993). If fitted with a power law, the derived energy spectral index is steep, with an average value of $\alpha = 1.7$, but the observations are also consistent with thermal models with temperatures around 50–100 keV. The spectra resemble those from Galactic black hole candidates spectra, observed by OSSE and SIGMA, which show a thermal cutoff at high (~50–100 keV) energies (see e.g. Sunyaev et al. 1991, Stella 1992).

The Seyfert 1.5 galaxy NGC 4151 was detected by the SIGMA instrument on GRANAT in 1990 November, and the hard X-ray spectrum fitted by a power law of energy index $\alpha = 2.1^{+1.1}_{-0.9}$ above 40 keV (Jourdain et al. 1992). OSSE spectrum (almost one year later) can be fitted with a broken power law, with indices $\alpha = 1.1 \pm 0.3$ between 60 and 100 kev and $\alpha = 2.4^{+0.3}_{-0.4}$ between 100 and 500 keV. (Maisack et al. 1993). Coppi & Zdziarski (1992) have interpreted the SIGMA spectrum of NGC 4151 in terms of a non–thermal pair plasma model, where the steep hard X-ray spectrum is ascribed to both the effects of an intrinsic curvature in the primary spectrum of the non–thermal pairs, and the presence of a reflection Compton component, contributing mostly around 30 keV (Lightman & White 1988, George & Fabian 1991). In a subsequent paper, Zdziarski, Lightman & Maciolek (1993) have modified the non–thermal pair model for NGC 4151 to account for the OSSE results. In this version, only a fraction of the power

is injected in non–thermal particles, the remainder is released in a thermal component.

Altough the non–thermal pair model (for a review see Svensson 1992) predicts a steepening of the hard X-ray spectrum, the break cannot be as sharp as the OSSE data simply require. Furthermore, the non–thermal pair model predicts a flattening of the spectrum at $\sim 100-200$ keV, and the presence of a cospicuous annihilation line, neither of which is observed.

The steep spectra observed by OSSE can instead be interpreted on the basis of a thermal model, in which X–rays are due to multiple inverse Compton scatterings. In these models a strong constraint is due to the requirement of pair equilibrium (pair production balances annihilation and escape), which limits the possible temperature to a narrow range, which is weakly dependent on the compactness of the source (Svensson 1984, Zdziarski 1985). By compactness we mean the parameter $\ell = L\sigma_T/(Rm_ec^3)$, where $\sigma_T$ is the Thomson cross section and $L/R$ is the luminosity to size ratio. The resulting equilibrium temperature, for $\ell = 10$–$1000$, is of the order of 50–100 keV, which is tantalizingly close to the derived value from OSSE data.

The spectral shape produced by thermal plasmas depends upon the dominant radiation mechanism. Haardt & Maraschi (1991, 1993) have proposed a specific thermal model that naturally predicts a power law spectrum of index close to 0.8–1 below 40 keV and steeper above, by assuming that all the power is released in a hot corona above a relatively cold accretion disk. About half of the radiation emitted by the corona impinges onto the disk: the largest fraction of it is re–emitted as soft thermal radiation, while $\sim$ 10 per cent is Compton scattered to form the so-called Compton reflection hump The photons reprocessed by the disk are then the seed photons which are thermally Comptonized in the corona. Electron-positron pair production contributes to the optical depth, and limits the minimum possible optical depth and maximum allowed temperature.

The main result of the model is that the ratio between the Inverse Compton luminosity from the optically thin corona and the soft thermal luminosity from the underly-

ing opaque disk is fixed. This implies an almost constant Comptonization parameter of the order of 1. In this calculation we have found, for $\tau \lesssim 0.5$, $y = (16\Theta^2 + 4\Theta)\tau \simeq 0.6$. The energy spectrum of the IC component, averaged over positive angles, when approximated with a power law has, for a soft photon temperature of $kT_{\rm bb} = 50$ eV, a spectral index $\alpha = 0.9 \pm 0.05$, largely independent of the optical depth of the hot corona. This is in close agreement with the average value found for Seyfert galaxies after deconvolution of the reflection hump. For $kT_{\rm bb} = 5$ eV the spectrum of the IC component computed with the same approximation is only slightly steeper, $\alpha = 1.0 \pm 0.05$.

For $\tau \sim 1$ the Comptonization parameter is sensibly lower and the spectrum is steeper, $\alpha \gtrsim 1.2$. Present observations argue against optically thick coronae.

A more detailed computation of the expected spectra for different viewing angles, as appropriate for objects observed individually, and including the contribution of reflected photons, yields a larger spread in the spectral shapes. In the X-ray band, the spectra are flatter for smaller angles and higher soft photon energy. A reflection component is always present, but in different proportion with respect to the Comptonized component in the relevant energy range. These effects give rise to a diversity of predicted spectra which can account for the observed spectral index distributions of both, Seyfert galaxies and radio-quiet quasars, if the two classes have different $kT_{\rm bb}$. In addition the thermal photon peak can be identified with the so called "soft excess" observed in several objects. All these features make the model extremely attractive for a "global" understanding of the high frequency emission of radio-quiet AGNs. Of course further reprocessing and absorption in external matter may add complexity to the observed spectra.

Finally it is interesting to note that, in the assumed geometry, the X-ray flux is expected to be polarized. Detailed calculations can be found in Haardt & Matt (1992), where it is shown that the degree of polarization is a strong function of the photon energy and of the viewing angle. In principle, future X-ray polarization observations can be used as a diagnostic for the two phase model.

### 1.1.2 Problems for Thermal Models: a possible solution

Thermal models have been previously criticized as the root cause of the high energy spectrum of AGN, mainly because of the long thermalization time needed at high temperatures. Observed X-ray variability timescales are often so short, indeed less than the inferred 2-body thermalization timescales, that doubt is cast on the possibility that the plasma can be described by a Maxwellian distribution. There are therefore significant problems with both the thermal and non–thermal models for the hard X-ray spectra.

However in a recent paper (Ghisellini, Haardt & Fabian 1993) I gave reasons why the emitting particle energies extend to low values, and calculate in a self consistent way the expected spectrum. This is achieved by assuming a mechanism which re–injects particles, once cold, at some given energy $\gamma_0 m_e c^2$ (for an extended discussion on reacceleration models, see Done, Ghisellini, & Fabian 1990, hereafter DGF, see also Cavaliere 1982 and Svensson 1987). If $\gamma_0$ is initially large, particles emit $\gamma$–rays which in turn create pairs, which are then reaccelerated. Assuming that the injected power is constant, the increased number of particles to be reaccelerated means that $\gamma_0$ decreases. Equilibrium is reached for $\gamma_0 \sim$ a few, when pair creation balances annihilation so that a constant number of particles is reaccelerated: the equilibrium value of $\gamma_0$ is a few, and only weakly dependent on the compactness. With this hypothesis the entire equilibrium particle and photon distributions have been derived, which (as in completely thermal plasmas) are functions only of the compactness of the source.

These results show what happens if acceleration/heating continues in the emission region and involves *all* the particles present. Standard non–thermal models calculate the spectrum resulting from a region in which only a small and constant number of particles are accelerated and cool, despite the fact that pair production increases the total number of particles present. Standard thermal models assume that all particles are heated and maintained in a Maxwellian distribution at constant temperature (which depends on the particle density), despite the rapid variations in luminosity that are observed. Our

model lies between these extremes, since it responds to the varying particle density, and allows the particles both to cool and to be non–Maxwellian.

Our model can accounts for the general observations of high energy emission of compact sources. In this model the particle distribution (computed self consistently) is basically non–thermal, but extends in energy up to only a few MeV. We followed the treatment of DGF by assuming that throughout the source energetic pairs are injected monoenergetically at some Lorentz factor $\gamma_0$, at a rate corresponding to the compactness $\ell_h$. Soft (UV) photons are injected at a rate corresponding to a compactness $\ell_s$, with a blackbody spectrum of temperature $kT_{BB}$. The injected particles cool by Compton scattering, then join a thermal distribution at some temperature $kT$, and finally part of them annihilate, while the remaining are reaccelerated back to $\gamma_0$ and reinjected. We assumed that the plasma is pair dominated, i.e. that the pairs outnumber protons, and that the plasma is in pair equilibrium, i.e. the rates for pair creation and pair annihilation balance. Neglecting escape, the assumption of pair equilibrium gives $\tau_T$ as (e.g. Svensson 1987)

$$\tau_T = \left(\frac{4}{\pi}\xi\ell\right)^{1/2} \tag{1.1}$$

where $\xi$ is the pair yield, i.e. the ratio of the luminosity in pair rest mass to the total injected luminosity. The pair yield measures the efficiency of the source to convert the injected power in pair rest mass.

We assumed that the reaccelerator operates on all particles, once cooled, on the timescale $t_r$. The reacceleration process takes particles of $\gamma \sim 1$ and reinjects them at $\gamma_0$, with a total power given by

$$L_h = V m_e c^2 (\gamma_0 - 1)\frac{N}{t_r} \tag{1.2}$$

where $V$ is the volume of the source, assumed spherical, and $N$ is the density of the cold particles, i.e. $N = \tau_T/(\sigma_T R)$. The reacceleration time was taken to be equal to $t_{cool}$

which in turn is calculated assuming cooling by Compton scattering and Coulomb collisions. In other words, we required that the pairs can cool before being re–accelerated. The above equations suffice to solve for the equilibrium values of $\tau_T$ and $\gamma_0$ once the pair yield, $\xi$, is known. The resulting scattering optical depth of the relativistic particles was found to be equal to $\tau_T$, making the total depth equal to twice $\tau_T$.

DGF have calculated the pair yield as a function of $\gamma_0$, and have interpolated the numerical results with a simple analytical prescription, which was intended to described the overall behaviour of $\xi(\ell, \gamma_0)$ also for large $\gamma_0$. Based on their results (see their Fig. 1), we here introduce another simple prescription, modelled to better represents $\xi$ in the range $1 < \gamma_0 < 10$

$$\xi = 0.01 \left(\frac{\gamma_0}{10}\right)^3 \left(\frac{\ell_h}{\ell_s}\right)^{1/2} \min\left(1, \frac{\ell_h}{30}\right) , \qquad \ell_h \geq \ell_s \tag{1.3}$$

This is a crude approximation to the exact pair yield, but is sufficient for our scope, since the dependence of the equilibrium $\gamma_0$ on $\xi$ is weak. Once we know $\gamma_0$ and $\tau_T$, we derive the particle distribution assuming cooling by Compton scattering and by Coulomb collisions. At low energies, the latter process establishes a Maxwellian distribution, whose temperature is derived by balancing the heating due to Coulomb collisions of relativistic particles with the cooling due to thermal Comptonization. We assume that the relative contribution of thermal particles to the spectrum can be approximated with $(2/3)[\exp(y_M) - 1]$, where $y_M = 4\Theta\tau_T(1 + 4\Theta)(1 + \tau_T)$. The factor 2/3 has been introduced to match Monte Carlo results for $y_M$ smaller than a few. In this way we can find the equilibrium $\Theta$ which, in the cases studied here, is always greater than the Compton temperature. This is because of the large energy exchange between relativistic and thermal particles. In other words, Coulomb collisions between the two populations of particles is a more efficient process than the heating due to the collisions of cold particles with high energy photons. At high energies there is a tail of quasi power–law shape, resulting from injection and cooling. This distribution is calculated by the

continuity equation. In Fig. 1.a the main electrons parameters are shown (from top to the bottom $\gamma_0$, $\Theta$ and $\tau_T$. In Fig. 1.b the electron distribution is shown for the case $\ell_h = 100$.

We have assumed $\ell_h/\ell_s = 2$, and we have added to the primary spectrum a Compton reflection component due to cold matter intercepting half of the primary radiation, as in the case of an illuminated cold disk. Note that the choice of $\ell_h/\ell_s = 2$ mimics the case of a plane parallel corona model, in which all the power is released in the corona above the disk (as in the model of Haardt & Maraschi 1991). Spectra are then computed with a Montecarlo code.

The roll–off of the primary spectrum at energies greater than 100 keV (due to the small $\gamma_0$), and the contribution of the 'reflection' component produces a break of the spectrum at $\sim$ 50 keV, with $\Delta\alpha \sim 1$. The average shape of the spectrum below the break depends only slightly on $\ell_h$, but depends on the ratio $\ell_h/\ell_s$, with flatter $\alpha$ increasing $\ell_h/\ell_s$. Vice versa, the shape of the spectrum above 50 keV depends on $\ell_h$, being steeper for larger $\ell_h$, because of the smaller $\gamma_0$.

We have shown that reacceleration of low energy pairs at a rate equal to their cooling rate can yield a particle distribution extending in energy to a few MeV. It consists of a Maxwellian at low energies, followed by a quasi–power–law tail at high energies. Since the maximum energy is small, the overall photon spectrum produced by multiple Compton scattering resembles spectra produced by thermal plasmas.

For hard to soft compactness ratios close to 2 the overall spectral energy index is close to unity up to 100 keV, and steeper above. Addition of the Compton reflection hump flattens the spectrum below 50 keV and steepens it above. The spectra shown in Fig. 2 can explain both the existing observations of Seyfert galaxies in the 2–20 keV band and the spectra recently observed by OSSE above 60 keV.

The reacceleration mechanism here proposed assumes that the plasma is pair dominated. If ambient, 'normal' plasma is also present, then the number density of reaccelerated particles would be greater than in the case here studied. Consequently, the

equilibrium $\gamma_0$ would be smaller. The values given here can then be considered as the maximum possible $\gamma_0$ at a given compactness. In this sense, our results are very similar to the classical results of completly thermal plasmas, where, for a given compactness, there exists a maximum allowed temperature.

We have also assumed that the reacceleration mechanism operates on cool particles. In the case of heating of hot particles, the resulting distribution is bound to peak at the energy where heating and cooling balances. Again, if pair equilibrium is required, this energy is small. The exact shape of that distribution depends on the details of the energy exchange process among particles in the peak. However the photon spectrum is very weakly dependent on the exact shape of the particle distribution, as long as the maximum particle energy is small.

We have assumed that the Comptonization source, approximated with a sphere, is surrounded by cold material giving rise to the Compton reflection component. This cold material could also produce the flux of soft photons if the power is primarily released in the hot plasma, as in the model of Haardt & Maraschi (1991, 1993). If the hot component is above a cold disk, then one should also consider the effect of Compton anisotropy, which here has been neglected for simplicity (see e.g. Ghisellini et al. 1991, Haardt 1993). It would introduce a line–of–sight dependence of the spectrum and of the total power, the disk receiving more power than the observer. Therefore the reflection hump is increased with respect to the cases shown here, with minor modifications also in the incident spectrum (Haardt & Maraschi 1993).

One of the main overall features of our study is that intense and repeated heating of a compact emission region results in a pair–rich particle distribution which in turn yields a quasi–thermal emergent photon spectrum. The basic results obtained in the thermal scenario (e.g. Sunyaev & Titarchuck 1980, Svensson 1984, Zdziarski 1985, Haardt & Maraschi 1991, 1993) are not significantly altered if the Maxwellian prescription is dropped. The use of a thermal electron distribution is then justified from a computational point of view, keeping in mind that the temperature should be consid-

ered as a measure of the mean energy of the actual electron distribution, rather than a thermodynamical quantity.

## 1.2 GBH: CYGNUS X-1

Cyg X–1 is the brightest of the Galactic non–transient black hole candidates, and its X–ray spectrum has been well studied (see e.g. the review by Liang & Nolan 1984). It shows a hard power law in the 2–10 keV band, and excess emission at lower energies which is thought to arise from thermal emission from the accretion flow. The high energy cutoff in the spectrum at $\sim$ 100 keV suggests a thermal energy distribution of the X–ray emitting particles, leading to the widespread use of optically thick thermal Comptonization models to describe the X–ray spectrum in this and other black hole candidates.

If X–rays illuminate an optically thick accretion flow, as expected if it forms an accretion disk, a Compton reflection spectrum is formed, whose signatures are a broad hump, peaking between 10–100 keV, a strong Fe K edge, and an associated Fe K$\alpha$ emission line (Guilbert & Rees 1988; Lightman & White 1988). These spectral features also provide a diagnostic of the ionization state of the material, as the photoelectric opacity decreases with ionization, enhancing the low energy reflected flux (Lightman & White 1988), increasing the energy of the iron edge and line (e.g. Makishima 1986) and changing the line equivalent width (Ross & Fabian 1993; Matt, Fabian & Ross 1993).

The characteristic spectral features of reflection have been clearly seen in both Active Galactic Nuclei (AGN, e.g. Pounds et al. 1990; Matsuoka et al. 1990) and black hole candidates (Tanaka 1991; Ebisawa 1991; Done et al. 1992). While this reinforces the analogy between these two classes of objects (White, Fabian & Mushotzky 1984), it also reveals some subtle differences. In AGN the Fe K$\alpha$ emission line (generally with an equivalent width, $W_\alpha$, of 100-200 eV: e.g. Nandra 1991) and reflected continuum are in general consistent with that predicted from a flat, solar abundance, cold X–ray

illuminated disk (George & Fabian 1991; Matt, Perola & Piro 1991). However, in Cyg X–1 the iron edge energy implies that the material is significantly ionized, while the (poorly determined) equivalent width of the line is about 50 eV, like in other Galactic black hole systems (Ebisawa 1991; Done et al. 1992; Mitsuda 1992).

There are two ways to reduce $W_\alpha$. The first is by resonant absorption followed by Auger de-excitation (Ross & Fabian 1993); this is an efficient way only for iron between FeXVIII–FeXXIII, as Auger ionization is suppressed for highly ionized ions. If the source is point–like, and the disk is "cold", this range of ionization states is obtained only in a small region of the disk (Matt et al. 1993). For typical temperatures in the disk inner region in stellar mass black holes, such ionization states can be present over a larger area, due to collisional ionization. However, an extended source is more effective in reducing the line intensity, as here the ionizing flux is constant over large areas of the disk. The second way is through Compton scattering. If the Comptonizing corona extends over the disk, only part of the line photons will escape unscattered towards the observer. The remainder is Compton scattered, leading to substantial broadening (e.g. Podznayakov, Sobol & Sunyaev 1983), so that they would be lost under the continuum in any present day X–ray detector. This again requires a covering factor of order unity, suggesting the geometry of this Comptonizing region to be that of an extended corona over the disk.

In such a physical picture the blackbody photons from the disk, the line and reflection continuum must all pass through the corona. This alters the theoretical predictions for both the shape and normalization of the reprocessed components in a manner which depends in particular on the Thomson depth of the corona, $\tau_{\rm T}$. In order that any reflected features are detectable at all implies that $\tau_{\rm T}$ <1. This is significantly smaller that that predicted by fitting simple "Comptonization–only" models to the spectrum of Cyg X-1, where $\tau_{\rm T}$ ~3 is typically found (e.g. Sunyaev & Titarchuk 1980). A corona with that Thomson depth would smear out any reflected features into invisibility.

For archival EXOSAT GSPC data from Cyg X–1, the parameters Haardt et al.

(1993), in the framework of a plane parallel Comptonization model (Haardt 1993) obtained are $\tau_{\rm T} \sim 0.3$ and $kT_{\rm e} \sim 150$ keV. While the models were computed for a wide range of parameter values, only certain solutions are physically self–consistent in terms of balancing the heating and cooling processes. Remarkably, the best fit parameters are consistent with those derived from equilibrium solutions. These coronal parameters are also compatible with the high energy data, such as that observed by the SIGMA and OSSE instruments, though the reported optical depth and electron temperature for these data are very different. This apparent discrepancy is due to the common use of optically thick plasma models (e.g. Sunyaev & Titarchuk 1980); if the source is in fact optically thin, as suggested by the actual detection of the reflection component, the temperature is underestimated by a factor of $\sim$3, and so the optical depth is overestimated by a factor 5–10.

## REFERENCES

Balucinska M., Hasinger G., 1991, A&A, 241, 439

Cameron R.A. et al., 1993, to be published in the proceedings of the Compton symposium, St. Louis, MO, ed. N. Gehrels

Cavaliere A., 1982, in Plsama Astrophysics, SP–161, ESA, p.97.

Chandrasekhar S., 1960, Radiative Transfer. Dover, New York

Comastri A., Setti G., Zamorani G., Elvis M., Giommi P., Wilkes B. J., Coppi P., Zdziarski A. A., 1992, ApJ, 398, L37

Dolan J. F., Tapia S., 1989, ApJ, 344, 830

Done C., Mulchaey J. S., Mushotzky R. F., Arnaud K. A., 1992, ApJ, 395, 275

Done C., Ghisellini G., Fabian A. C., 1990, MNRAS 245, 1

Done C., Fabian A. C., 1990, MNRAS, 240, 81

Ebisawa K., 1991. PhD Thesis, University of Tokyo, Japan

Field G. B., Rogers R. D., 1992, in Holt S. S., Neff S. G., Urry C. G., eds, Proc. of Conf., Testing the AGN Paradigm. AIP, New York, p. 329

Field G. B., Rogers R. D., 1993, ApJ, 403, 94

Frontera F., Dal Fiume D., 1992, in Koyama K., Kunieda H., eds, Proc. of Conf., Frontiers of X–ray Astronomy. Universal Academy Press, Tokyo, p. 311

George I. M., Fabian A. C., 1991, MNRAS, 249, 352

Ghisellini G., George I. M., Fabian A.C., Done C., 1991, MNRAS 248, 14

Ghisellini G., Haardt F., Fabian A. C., 1993, MNRAS, 263, L9

Gies D. R., Bolton C. T., 1986, ApJ, 304, 371

Grabelsky D.A., et al., 1993. To appear in the Proc. of the First Compton Observatory Symposium, St. Louis, October 1992

Guilbert P. W., Fabian A. C., Stepney S., 1982, MNRAS, 199, 19P

Guilbert P. W,. Rees M. J., 1988, MNRAS, 233, 475

Haardt F., Maraschi L., 1991, ApJ, 380, L51

Haardt F., Maraschi L., 1993, ApJ, 413, 507

Haardt F., 1993, ApJ, 413, 680

Haardt F., Done C., Matt G., Fabian A. C., 1993, ApJ, 411, L95

Haardt F., Matt G., 1993, MNRAS, 261, 346

Hua X.-M., Lingenfelter R. E., 1992, ApJ, 397, 591

Jourdain E. et al., 1992, A&A, 256, L38

Liang E. P., Nolan P. L., 1984, Space Sci. Rev., 38, 353

Lightman A. P., White T. R., 1988, ApJ, 335, 57

Maisack et al. 1993, ApJ, in press

Makishima K., 1986, in Mason K.O., Watson M.G., White N.E., The Physics of Accretion onto Compact Objects. Springer-Verlag, Berlin, p. 249

Matsuoka M., Piro L., Yamauchi M., Murakami T., 1990, ApJ, 361, 440

Matt G., Perola G. C., Piro L., 1991, A&A, 247, 25

Matt G., Perola G. C., Piro L., Stella L., 1992, A&A, 257, 63, (erratum: 1992, A&A, 263, 453)

Matt G., Perola G.C., Stella L., 1993, A&A, 267, 643

Matt G., Fabian A. C., Ross R., 1993, MNRAS, in press

Mitsuda K., 1992, in Koyama K., Kunieda H., eds, Proc. of Conf., Frontiers of X–ray

Astronomy. Universal Academy Press, Tokyo, p115

McDowell J. C., 1992, ApJ, 384, 62

McHardy I. M., 1989, in Hunt J., Battrick B., eds, Proc. of 23rd ESLAB Sypm., Two Topics in X-Ray Astronomy. ESA SP-296, p. 1111

Morrison R., McCammon D., 1983, ApJ, 270, 119

Mushotzky R. F., 1984, Adv.Sp.Res., 3, 157

Nandra K., Pounds K. A., Stewart G. C., Fabian A. C., Rees, M. J., 1989, MNRAS, 236, 39P

Nandra K., 1991, Ph.D. Thesis, Leicester University

Nishimura J., Mitsuda K., Itoh M., 1986, PASJ, 38, 819

Nolan P.L., Gruber D. E., Knight F. K., Matteson J. L., Rothshild R. E., Marshall F. E., Levine A. M., Primini F. A., 1981, Nat, 293, 275

Perotti F. et al., 1986, ApJ, 300, 297

Pounds K. A., Nandra K., Stewart G. C., George I. M., Fabian A. C. , 1990, Nat, 344, 132

Pounds K. A., Nandra K., Stewart G. C., 1992, in Brinkmann W., Truper J., eds, Proc. of Conf., X-Ray Emission from AGN and the Cosmic XRBG. MPE report 235, Garching, p. 1

Pozdnyakov L. A., Sobol' I. M., Sunyaev R. A., 1983, Ap. Space Sc. Rev., Vol. 2, p. 189

Ross R. R., Fabian A. C., Mineshige S., 1992, MNRAS, 258, 189

Ross R. R., Fabian A. C., 1993, MNRAS, 261, 74

Rybicki G. B., Lightman A. P., 1979, Radiative Processes in Astrophysics. Wiley, New York

Salotti L. et al., 1992, A&A, 253, 145

Spitzer L., 1956, Physics of Fully Ionized Gases, Wiley, New York

Stepney S., 1983, MNRAS, 202, 467

Stella L., 1992, in: 13th International Conference on General relativity and Gravitation, Argentina, July 1992, (IOP Publishing: Bristol) Ed. C. Kozameh, in press

Sunyaev R. A., Titarchuk L. G., 1980, A&A, 86, 121

Sunyaev R. A., Titarchuk L. G., 1985, A&A, 142, 374

Sunyaev R. A., Trumper J., 1979, Nat, 279, 506

Sunyaev R. A. et al., 1991, Sov. Astron. Lett., 17, 409

Svensson R., 1984, MNRAS, 209, 175

Svensson R., 1987, MNRAS, 227, 403

Svensson R., 1992, in X–Ray Emission from Active Galactic Nuclei and the Cosmic X–ray Background, eds. W. Brinkmann & J. Trümper (MPE report 235) 103

Tanaka Y., 1991, in Treves A., Perola G. C., Stella L., eds, Proc. of Diagnostics in X–ray Sources. Springer–Verlag, Berlin, p80

Turner T. J., Pounds K. A., 1989, MNRAS, 240, 833

Ubertini P., 1991, ApJ, 366, 544

Urry C. M., Arnaud K., Edelson R. A., Kruper J. S., Mushotzky R. F., 1989, in Hunt J., Battrick B., eds, Proc. of 23rd ESLAB Sypm., Two Topics in X-Ray Astronomy. ESA SP-296, p. 789

Walter R., Courvoisier T. J.-L., 1992, A&A, 258, 255

White N. E., Fabian A. C., Mushotzky R. F., 1984, A&A, 133, L9

White T. R., Lightman A. P., Zdziarski A. A., 1989, ApJ, 331, 939

Williams O. R. et al., 1992, ApJ, 389, 157

Zdziarski A. A., 1985, ApJ, 289, 514 (Z85)

Zdziarski A. A., Ghisellini G., George I. M., Fabian A. C., Svensson R., Done C., 1990, ApJ, 363, L1

Zdziarski, A.A., Lightman, A.P. & Maciolek–Niedzwiecki, A. 1993, ApJ, in press

## FIGURE CAPTIONS

**Figure 1.** Upper panel shows different electron parameters as a function on the source compactness. The hard/soft ration is 2. The curves represent (from top to the bottom) the maximum Lorentz factor ($\gamma_0$), the decreasing Maxwellian temperature ($\Theta$) and the increasing optical depth due to Maxwellian elctrons ($\tau_T$). The lower panel shows the electron momentum distribution for the case $\ell = 100$. Solid line is the total ditribution, dashed line is the low temperature maxwellian, and dotted line is the cooled power law.

**Figure 2.** Comptonization spectra computed with a Monte Carlo code, assuming the particle distribution calculated as described in the text, for compactness values of $\ell_h = 10$, 100 and 1000, and $\ell_h/\ell_s = 2$. The parameter for the three models are, in order of increasing compactness: $\tau_T = 0.09$, 0.23, 0.46; $\gamma_0 = 5.8$, 3.4, 2.5; $\Theta = 0.42$, 0.18, 0.06. To the direct Comptonization spectrum (dashed line), we have added a 'Compton reflection' component, calculated assuming $\Omega/2\pi = 1$ and cold neutral matter with solar abundance. The total resulting spectrum is shown as a solid line. For reference, we have drawn a line of slope 0.7 between 2 and 10 keV, and a line of slope 1.7 between 60 and 300 keV.

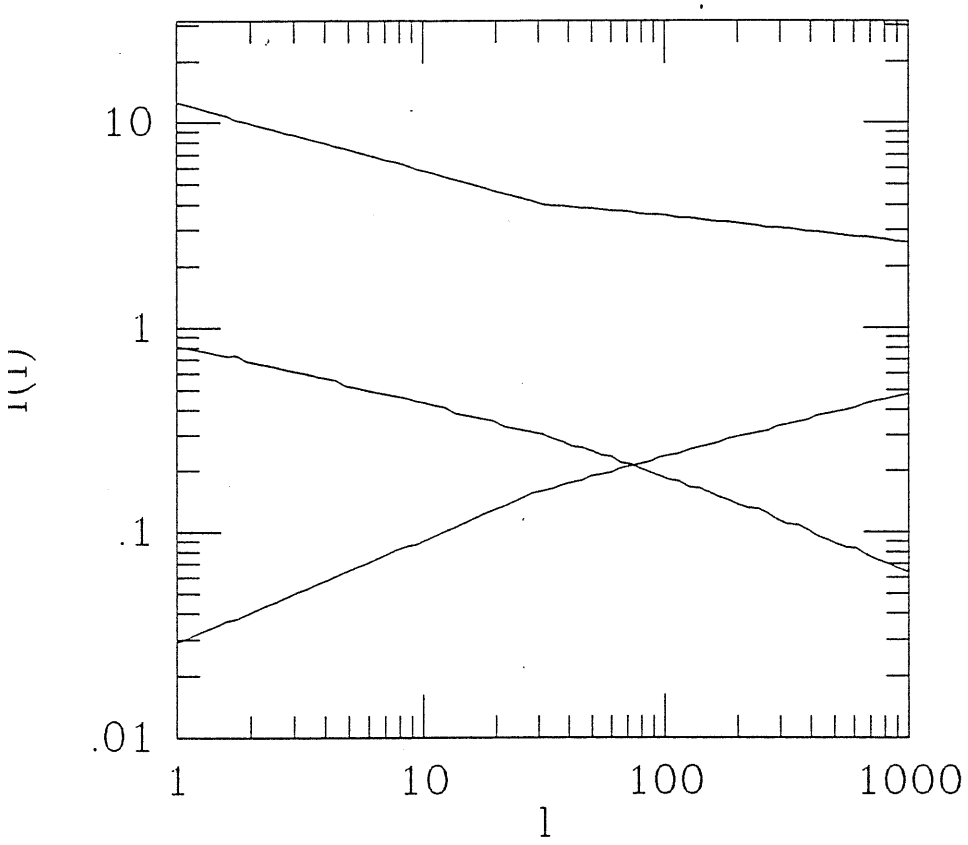
10
1
.1
.01
1
10
100
1000
l
I(l)

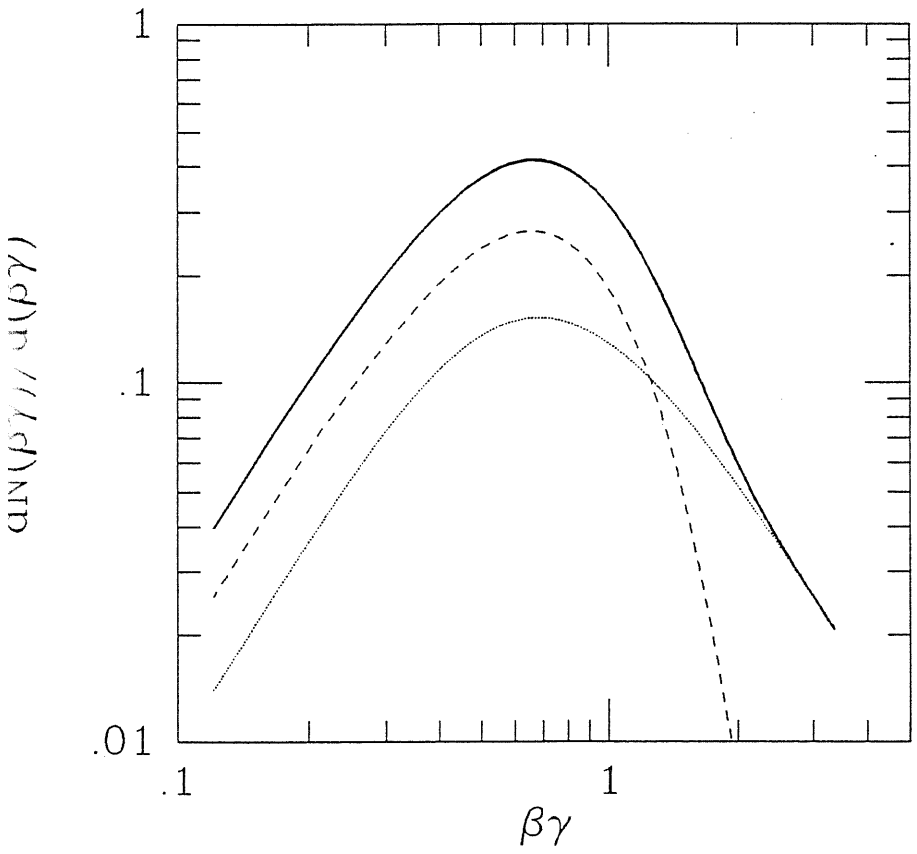
1
.1
.01
.1
1
βγ
dN/(βγ)

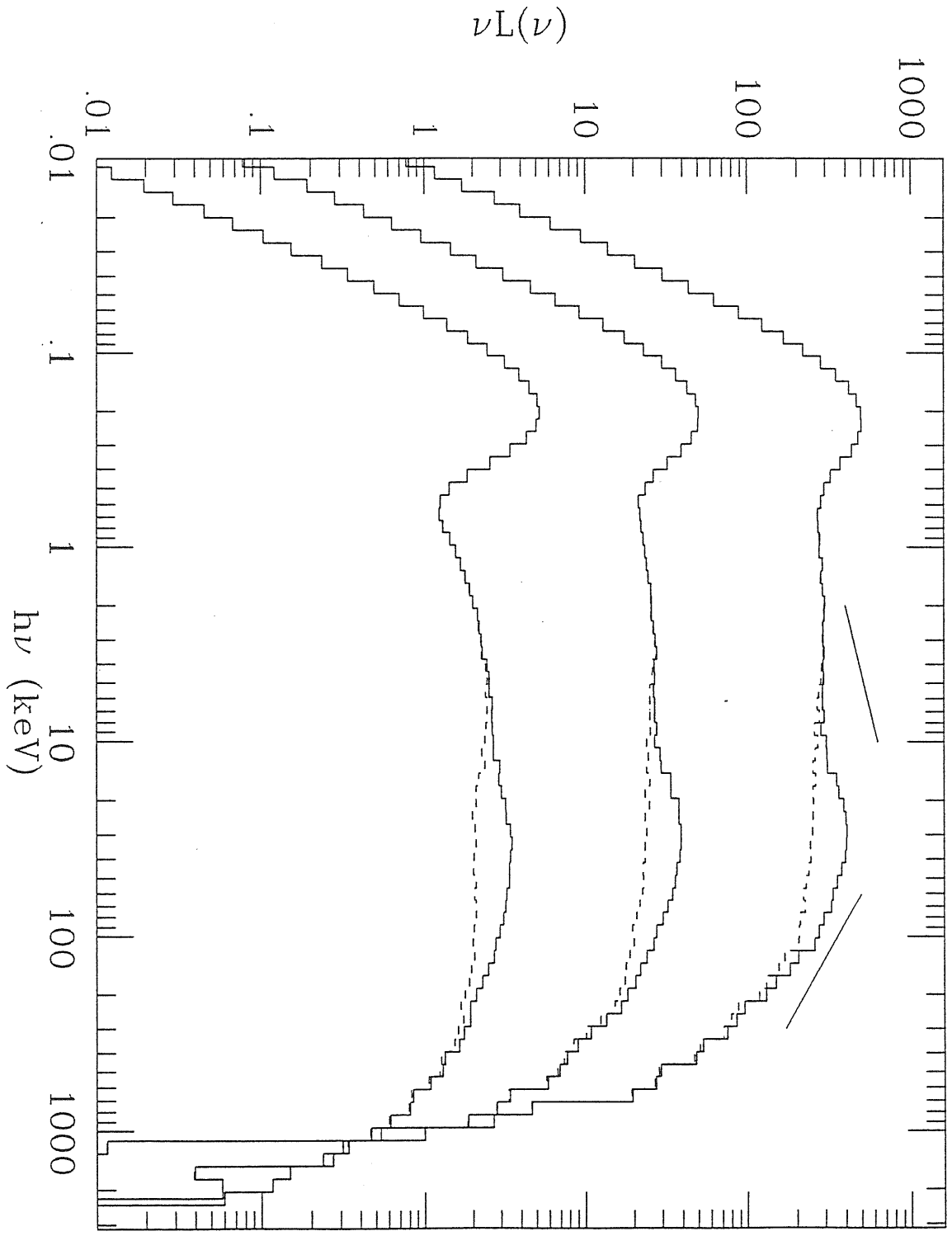
$\nu L(\nu)$
.01
.1
1
10
100
1000
$h\nu$ (keV)
.01
.1
1
10
100
1000

# Chapter 2

# Theory

*The basic equations of Compton scattering are reviewed. The kinetik equation is solved iteratively, by means of an isotropic kernel. I show examples of calculations for two 1-D geometries, namely an homogeneous sphere, and a plane parallel slab. The special case of Thomson scattering is discussed. The formalism is then developed for treating anisotropic Inverse Compton emission, with particular emphasis to the thermal case.*

## 2.1 BASIC EQUATIONS

The theory of Compton scattering is well established, and a complete discussion with astrophysical applications can be found for example in Pozdniakov, Sobol & Sunyaev (1983). A basic reference for an overview of the topic in an astrophysical context is Rybicki & Lightman (1979).

Here we simply recall that the momentum $\mathbf{x}' \equiv (h\nu'/c)\mathbf{\Omega}'$ of a photon scattered by an electron of momentum $\mathbf{p} \equiv \gamma m_e \mathbf{v}$ is changed into $\mathbf{x} \equiv (h\nu/c)\mathbf{\Omega}$ where

$$\frac{\nu}{\nu'} = \frac{1-\mu'\beta}{1-\mu+(h\nu'/\gamma m_e c^2)(1-\cos\alpha)} \tag{2.1}$$

Here $\beta \equiv v/c$, $v \equiv |\mathbf{v}|$, $\mu \equiv \mathbf{\Omega}\cdot\mathbf{v}/v$, $\mu' \equiv \mathbf{\Omega}'\cdot\mathbf{v}/v$, and the scattering angle

$\alpha \equiv \cos^{-1}(\Omega \cdot \Omega')$.

If the photon is scattered by an electron at rest, its frequency changes because of the recoil effect, and in general the electron gains energy. This is often referred as Direct Compton effect. Otherwise, if the electron is moving at high speed, the Doppler effect plays a dominant role, and the photon can gain energy. This effect is called Inverse Compton. This is likely to be the main high energy photon production mechainism in compact sources.

The differential cross section of this process can be written as

$$\frac{d\sigma}{d\Omega} = \frac{3\sigma_T}{16\pi\gamma^2} \frac{W}{(1-\mu'\beta)^2} \left(\frac{\nu}{\nu'}\right)^2 \tag{2.2.a}$$

where

$$\begin{aligned} W &\equiv \frac{w}{w'} + \frac{w'}{w} + 2\left(\frac{1}{w'} - \frac{1}{w}\right) + \left(\frac{1}{w'} - \frac{1}{w}\right)^2 \\ w &\equiv \gamma x(1-\mu\beta) \\ w' &\equiv \gamma x'(1-\mu'\beta) \end{aligned} \tag{2.2.b}$$

Here $x \equiv h\nu/m_e c^2$ and $x' \equiv h\nu'/m_e c^2$ .

The total cross section is expressed by the Klein-Nishina formula:

$$\sigma(w) = \frac{3\sigma_T}{8w}\left[\left(1 - \frac{2}{w} - \frac{2}{w^2}\right)\ln(1+2w) + \frac{1}{2} + \frac{4}{w} - \frac{1}{2(1+2w)^2}\right] \tag{2.3}$$

It is important to recall that the *effective* probability of scattering for a photon with a beam of electrons moving at speed v is proportional to

$$\sigma_{\text{eff}}(w) \equiv (1-\mu\beta)\sigma(w) \tag{2.4}$$

For example, the scattering probability for a photon moving parallel ($\mu = 1$) to an ultrarelativistic electron beam, is $\sim 0$.

## 2.2 COMPTONIZATION SPECTRA

### 2.2.1 General Outline

The term *Comptonization* generally indicates a process where multiple scatterings play a major role in forming the resulting radiation spectrum. The evolution of the photon occupation number in the phase space is described by the Boltzmann kinetik equation. The Boltzmann equation may be expanded to second order if the fractional energy transfer per scattering is small. This is the case for nonrelativistic electrons. If the electron distribution is thermal, the resulting equation is known as *Kompaneets* equation, reading:

$$\frac{\partial n}{\partial t_c} = \frac{\Theta}{x^2}\frac{\partial}{\partial x}[x^4(n' + n + n^2)] \tag{2.5}$$

where $x \equiv h\nu/m_e c^2$, $n' \equiv \partial n/\partial \mathrm{x}$ and $\Theta \equiv kT_e/m_e c^2$. The quantity $t_c \equiv (n_e \sigma_T c)t$ is the time in units of mean scattering time. Note that the mean scattering time is the light crossing time $R/c$ divided by the scattering optical depth $\tau \equiv n_e \sigma_T R$. A solution to the Kompaneets equation has been obtained by Sunyaev & Titarchuk (1980) in the diffusion approximation. The resulting analytical solutions are valid for $\Theta \lesssim 0.3$, and for optical depth $\tau \equiv n_e \sigma_T R \gtrsim 3$, where $R$ is the size of the scattering medium. This solution is of great importance, as it provides an anlytical description of Comptonization. The Sunyaev & Titarchuk model is widely used in fitting the high energy spectrum of galactic and extragalctic sources (refs.). However, as seen in §? the problem of Comptonization in rarefied ($\tau < 1$) hot plasmi is of main interest in astrophysics. Mild-relativistic and relativistic IC scattering is thought to be responsible of the intense X–ray and $\gamma$–ray emission observed in GBHC and AGN. The lack of a suitable analytical formulation in these situations led to an intense use of numerical simulations. An analytical approach can be however carried out in rather generic situations, solving the kinetik equation iteratively, i.e. computing the photon distribution within the medium after each scattering event. Appropriate boundary conditions are then used to evaluate the observed radiation spectrum.

### 2.2.2 Iterative Solution

Consider a given initial photon distribution $(x\Omega, \mathbf{r})$ a point in the photon phase space, where $x$ is the photon energy in adimensional units, $\Omega$ is a unit vector parallel to the photon momentum, and $\mathbf{r}$ a point in an Euclidean reference system.

The distribution $T_0$ is the *0-th order source function.* It defines the seed photon distribution in the phase space. Our task is to calculate the evolution of this distribution due to electron scattering within a finite medium of volume $\mathcal{V}$.

Photons created in $\mathbf{r}'$ with momentum $\mathbf{x}$ can well suffer a scattering along the straight flight toward the boundary of the medium before escaping. We are interested in the number of photons of momentum $\mathbf{x}$ that are going to be scattered by an electron located in $\mathbf{r}$. The scattering probability can be easily computed, so that we can write the *1-st order source function* as:

$$T_1(x\Omega, \mathbf{r}) = \int_{\mathcal{V}} d\mathbf{r}'\, T_0(x\Omega, \mathbf{r}')\, \mathrm{e}^{-|\mathbf{r}'-\mathbf{r}|} \qquad (2.6.a)$$

where the integral is performed over the source volume. Note that $\Omega \equiv (\mathbf{r}-\mathbf{r}')/|\mathbf{r}-\mathbf{r}'|$. The spatial coordinate is implicitly measured in units of $n_e\sigma$.

Of course a photon created in $\mathbf{r}'$ has also a non zero probability to escape unscattered from the medium. The $S_0(\mathbf{x})$, i.e. the 0-th scattered *observed* spectrum, can be written as

$$S_0(x\Omega) = T_1(x\Omega, \mathbf{R}) \qquad (2.6.b)$$

It is now obvious that $T_1$ plays the same role than $T_0$, but with a main difference: now $\mathbf{r}$ becomes a point-source of "new" photons, whose momentum distribution is changed according to the scattering laws. The new momentum distribution can be computed by means of a *kernel* $K_P(x\Omega, x'\Omega') \equiv P[(x'\Omega') \rightarrow (x\Omega)]$, describing the probabability that the photon momentum changes from $x'\Omega'$ to $x\Omega$ because scattering.

Of course the kernel depends also on the electron momentum, albeit not explicity indicated. As discussed in the next section, the electrons are generally assumed to have a randomly oriented momentum. This kernel is then averaged over the (given) electron energy distribution.

The scattered photons "created" in $\mathbf{r}'$ again have a non zero probability to be furtherly scattered by an electron located in $\mathbf{r}$ along the straight line $(\mathbf{R}' - \mathbf{r}')$, where $\mathbf{R}'$ defines the source boundary. In the same way as eq.[2.6.a] we can compute $T_2(x\mathbf{\Omega}, \mathbf{r})$ as

$$T_2(x\mathbf{\Omega}, \mathbf{r}) = \int_{\mathcal{V}} d\mathbf{r}' \, \mathrm{e}^{-|\mathbf{r}'-\mathbf{r}|}, \int_{\mathcal{P}} d(x'\mathbf{\Omega}') \, K_{\mathcal{P}}(x\mathbf{\Omega}, x'\mathbf{\Omega}') \, T_1(x'\mathbf{\Omega}', \mathbf{r}') \qquad (2.7.a)$$

where again $\mathbf{\Omega} \equiv (\mathbf{r}-\mathbf{r}')/|\mathbf{r}-\mathbf{r}'|$. The second integral in the above equation is performed over space $\mathcal{P}$ of photon momenta.

Again, some of the single scattered photons will escape from the source without suffering the second scattering. Their distribution $S_1(x\mathbf{\Omega})$, i.e. the 1-st scattered *observed* spectrum, is simply given by

$$S_1(x\mathbf{\Omega}) = T_2(x\mathbf{\Omega}, \mathbf{R}) \qquad (2.7.b)$$

Now the argument can be repeated for any succesive scattering. It is now trivial to show that

$$T_{k+1}(x\mathbf{\Omega}, \mathbf{r}) = \int_{\mathcal{V}} d\mathbf{r}' \, \mathrm{e}^{-|\mathbf{r}'-\mathbf{r}|} \int_{\mathcal{P}} d(x'\mathbf{\Omega}') \, K_{\mathcal{P}}(x\mathbf{\Omega}, x'\mathbf{\Omega}') \, T_k(x'\mathbf{\Omega}', \mathbf{r}') \qquad (2.8.a)$$

and

$$S_k(x\mathbf{\Omega}) = T_{k+1}(x\mathbf{\Omega}, \mathbf{R}) \qquad (2.8.b)$$

Finally the emitted radiation spectrum $S(x\mathbf{\Omega})$is given by

$$S(x\mathbf{\Omega}) = \sum_{k=0}^{\infty} S_k(x\mathbf{\Omega}) \qquad (2.9)$$

It is interesting to consider the special case of Thomson scattering. When the cross section is indeed energy independent, the iterative solution described by eq.[2.8.a] and [2.8.b] can be carried out much more easily. Suppose that the initial distribution could be written as $T_0(x\Omega, \mathbf{r}) = X_0(x)J_0(\mathbf{r}, \Omega)$. Now it is easy to show that the evolution of the photon distribution in the space $\mathcal{P}$ can be separated from the pure spatial evolution in the volume $\mathcal{V}$. Then the k-th scattered observed spectrum can be written as

$$S_k(x\Omega) = p_k(\Omega)X_k(x\Omega) \tag{2.10.a}$$

where

$$\begin{aligned} p_k(\Omega) &\equiv J_{k+1}(\mathbf{R}, \Omega) \\ J_{k+1}(\mathbf{r}, \Omega) &= \int_{\mathcal{V}} d\mathbf{r}'\, J_k(\mathbf{r}', \Omega)\mathrm{e}^{-|\mathbf{r}'-\mathbf{r}|} \\ X_k(x\Omega) &= \int_{\mathcal{P}} d(x'\Omega')\, K_{\mathcal{P}}(x\Omega, x'\Omega')\, X_{k-1}(x'\Omega') \end{aligned} \tag{2.10.b}$$

The term $p_k(\Omega)$ represents the escape probability in direction $\Omega$ for a photon that has suffered k-th scatterings.

## 2.3 ENERGY AND SPACE EVOLUTION

### 2.3.1 Isotropic Kernel of Single Scattering

A great simplification can be made assuming that the scattering is isotropic *in the lab-frame*. As we will show in the next section, for the interesting range of the parameters this is a satisfactory approximation. This is a good assumption if the electron momenta are randomly oriented and if the input photons do not have a preferential direction. We call this condition *perfect isotropy*. In this case the kernel of single scattering depends only on the photon energies $x$, $x'$. Note that, if we assume an isotropic kernel, the observed spectrum *is not* in general independent from direction. In the following we will consider the case of isotropic scattering. The kernel $K_{\mathcal{P}}$ is then a function only of the energy of the photon before and after the scattering

The full relativistic kernel has been obtained by Jones (1968). Recentely Coppi & Blandford (1990) gave the correct formula of the kernel, as some equations in the Jones paper appear incorrect. This can be written as

$$K_{\mathcal{P}}(x,x',\gamma) = \int_{z_-}^{z_+} dz\, \frac{dP}{dz} \tag{2.11}$$

The inner differential function reads

$$\begin{aligned}\frac{dP}{dz}(x,x',\gamma) =& \frac{3\sigma_T\, cx}{16\gamma^4 x'^2 R(x',\gamma)(\beta^2+\epsilon^2+2\beta\epsilon z)^{1/2}(1-\beta z)} \\ &\times \Bigg[\!\!\Bigg[ 2y_0 k - ak^2 + (a^2-b^2)^{-1/2}(1+y_0^2-2ay_0k+a^2k^2) \\ &+ \frac{1}{k^2(1-\beta z)}\Bigg\{ k^2 + k^2(a^2-b^2)^{-1/2}\frac{a(2b-a)}{(a-b)} \\ &+ (a^2-b^2)^{-3/2}[a(1-y_0)^2 + 2kb^2(1-y_0) - ba^2k^2]\Bigg\}\Bigg]\!\!\Bigg]\end{aligned} \tag{2.12.a}$$

where $\epsilon = x'/\gamma$, $k = \gamma/x$, $a = 1-\beta z-(1-y_0)/k$, $b = \delta/k$ and

$$\begin{aligned} y_0 &= \frac{(\epsilon+\beta z)(\rho+\epsilon\rho-1+\beta z)}{\rho(\beta^2+\epsilon^2+2\beta\epsilon z)} \\ \delta &= \frac{\beta(1-z^2)^{1/2}[\rho^2\beta^2 + 2\rho\epsilon(1-\rho)(1-\beta z) - (\rho-1+\beta z)^2]^{1/2}}{\rho(\beta^2+\epsilon^2+2\beta\epsilon z)} \end{aligned} \tag{2.12.b}$$

with $\rho = x/x'$. The integration limits of eq.[2.11] are

$$\begin{aligned} z_- &= \max[\![-1, \beta^{-1}\{1-\rho[d+(d^2-1/\gamma^2)^{1/2}]\}]\!] \\ z_+ &= \max[\![+1, \beta^{-1}\{1-\rho[d-(d^2-1/\gamma^2)^{1/2}]\}]\!] \end{aligned} \tag{2.13}$$

where $d = 1+\epsilon-\epsilon\rho$.

The function $R$ in eq.[2.12.a] is the angle averaged scattering rate, i.e.

$$\begin{aligned} R(x,\gamma) &\equiv c\int_{-1}^{+1}\frac{d\mu}{2}\sigma_{\rm eff}(\mu) \\ &= \frac{3c\sigma_T}{16\gamma^2\beta x^2}\int_{\gamma x(1-\beta)}^{\gamma x(1+\beta)} dw\left[\left(1-\frac{2}{w}-\frac{2}{w^2}\right)\ln(1+2w)+\frac{1}{2}+\frac{4}{w}-\frac{1}{2(1+2w)^2}\right] \end{aligned} \tag{2.14}$$

It is important to note that the kernel defined above is normalized so as

$$\int_0^\infty dx K_{\mathcal{P}}(x, x', \gamma) = 1 \tag{2.15}$$

The kernel takes a very simple form if one neglect the electron recoil, and if the Thomson approximation is valid in the electron rest frame, i.e. if $x \ll \min(\gamma - 1,\, 1/\gamma)$. As shown by Rybicki & Lightman (1979) we find

$$K_{\mathcal{P}}(x, x', \gamma) = \frac{1}{4x'(\gamma^2 - 1)} \begin{cases} (1+\beta)\rho - (1-\beta) & \frac{1-\beta}{1+\beta} < \rho < 1 \\ (1+\beta) - \rho(1-\beta) & 1 < \rho < \frac{1+\beta}{1-\beta} \\ 0 & \text{otherwise} \end{cases}, \tag{2.16}$$

It may be easily checked that the kernel is normalized as eq.[2.15].

The average fractional energy gain is given by

$$\int_0^\infty dx (x - x') j(x) = \frac{4}{3}(\gamma^2 - 1) x' \ . \tag{2.17}$$

The approximated eq.[2.16] is obtained assuming an isotropic phase function for the scattering. The use of the more correct Ryleigh phase function gives negligible corrections.

In most of the interesting astrophysical situations, the scattering electrons are unlikely to be monoenergetic. In this case the kernel [2.11] (or [2.16]) needs to be averaged over the actual normalized electron distribution $N(\gamma)$, i.e.

$$K_{\mathcal{P}}(x, x') = \int_1^\infty d\gamma K_{\mathcal{P}}(x, x', \gamma) N(\gamma) \ . \tag{2.18}$$

### 2.3.2 Source volume integration

The geometry of the medium enters in the volume integrals of eq.[2.8.a]. For example we can consider an homogeneous sphere of scattering opacity $\tau \equiv n_e \sigma R$. This is the simpler case as the spectrum does not depend on direction. The angular intgeration can be easily carried out, and one can write the (k+1)-th source function as

$$T_{k+1}(x, r) = \int_0^\tau dr\, K_{\mathcal{V}}(r, r') \int_0^\infty dx'\, K_{\mathcal{P}}(x, x')\, T_k(x', r') \tag{2.19}$$

where

$$K_\nu(r,r') = \int_{-1}^{+1} d\mu \exp\left(r'\mu - \sqrt{r^2 - r'^2 + r'^2\mu^2}\right)$$
$$= \frac{1}{2r'}\Big\{(1+r+r')\mathrm{e}^{r'-r} - (1+r-r')\mathrm{e}^{-r'-r} \qquad (2.20)$$
$$+ (r^2 - r'^2)\left[\mathrm{E}_1(r+r') - \mathrm{E}_1(r-r')\right]\Big\}$$

for $0 < r' < r$ and

$$K_\nu(r,r') = \int_{-1}^{-\sqrt{r'^2-r^2}/r'} d\mu \Big[\exp(r'\mu + \sqrt{r^2 - r'^2 + r'^2\mu^2})$$
$$+ \exp(r'\mu - \sqrt{r^2 - r'^2 + r'^2\mu^2})\Big] \qquad (2.21)$$
$$= \frac{1}{2r'}\Big\{2(1 - \sqrt{r'^2 - r^2}\mathrm{e}^{-\sqrt{r'^2-r^2}} + (r + r' - 1)\mathrm{e}^{r-r'}$$
$$- (1 + r - r')\mathrm{e}^{-r-r'} + (r^2 - r'^2)\left[\mathrm{E}_1(r'+r) + \mathrm{E}_1(r'-r)\right]\Big\}$$

for $r < r' < \tau$. Here $\mathrm{E}_1$ indcates first order exponential integral function (e.g. Gautschi & Cahill 1970). Assuming that $T_0(x,r) = X_0(x)J_0(r)$, typical initial conditions are

$$J_0(r) = \frac{r^2}{3} \qquad (2.22)$$

for a homogenous seed photon source, and

$$J_0(r) = \delta(r - 0) \qquad (2.23)$$

for a point-like photon input in the centre of the sphere.

As the radial coordinate is in units of $n_e\sigma$, if the opacity depends on the photon energy the above expressions have different normalization for different photon energies. In order to avoid it, the function $K_\nu$ must be defined over an energy independent coordinate system. We can consider a unit sphere of radius $R = 1$, and then replace in [2.20] and [2.21] $r'$ with $\tau(x)r'$ and $r$ with $\tau(x)r$. The normalization of $K_r$ results correct for any photon energy $x$. The k-th observed spectrum must be written as

$$S_k(x) = \frac{T_{k+1}(x,1)}{\tau(x)} \qquad (2.24)$$

Another relavant 1-D case is a plane parallel geometry. Respect to the spherical case, a main difference is that even assuming isotropic scattering, the observed spectrum depends on the viewing angle. With $z$ we indicate the vertical coordinate along the slab. We find (see e.g. Nishimura, Mitsuda & Itoh 1986):

$$K_\nu(z,z') = \frac{1}{2}\mathrm{E}_1(|z-z'|) \tag{2.25}$$

The observed spectrum can be computed from

$$\begin{aligned} S_k(x,\mu) &= 2\int_0^\tau dz\, \mathrm{e}^{-(\tau-z)/\mu} \int_0^\infty dx'\, K_\mathcal{P}(x,x')\, T_k(x',z), \quad \mu \geq 0 \\ S_k(x,\mu) &= 2\int_0^\tau dz\, \mathrm{e}^{-z/|\mu|} \int_0^\infty dx'\, K_\mathcal{P}(x,x')\, T_k(x',z), \quad \mu \leq 0 \end{aligned} \tag{2.26}$$

## 2.4 ANISOTROPIC IC EMISSION

In the general case, the assumption of complete isotropy is unrealistic, because of the possible presence of an anisotropic soft photon input. A typical case is a plane parallel slab with the seed photon source located on the lower face. In this Section we drop the assumption of isotropy of the photon distribution; in this case the kernel depends on the angular variables.

Contrary to the case of complete isotropy, in which the fraction $dN$ of scattered photons per unit solid angle and their mean energy $lx\mathbf{r}$ are independent on direction, anisotropy implies an explicit dependence of $dN$ and $lx\mathbf{r}$ on $\Omega$. In the scattering process the electron radiative losses are larger (in the laboratory frame) in the backward direction of the input photons, and their magnitude depends on the electron energy (for a complete discussion see Ghisellini et al. 1991). It is important to point out that when the emission is integrated over the whole solid angle, we obtain exactly the same results as in the case of complete isotropy.

### 2.4.1 Anisotropy coefficients

In order to take the anisotropy effects into account, we consider a radiation beam. We can introduce two dimensionless coefficients, $\phi(\omega)$ and $\chi(\omega)$, representing the degree of anisotropy in the scattering event as function of the cosine of the scattering angle $\omega$. The coefficients are defined by the following relations:

$$dN = (1/4\pi)\phi(\omega)d\omega d\varphi \tag{2.27}$$

and

$$\langle x \rangle = [4/3(\gamma^2 - 1) + 1]\chi(\omega)x' \ . \tag{2.28}$$

By definition

$$\frac{1}{2}\int_{-1}^{1} d\omega\phi(\omega) = 1 \tag{2.29a}$$

and, defining $\xi(\omega) = \phi(\omega)\chi(\omega)$

$$\frac{1}{2}\int_{-1}^{1} d\omega\xi(\omega) = 1 \ . \tag{2.29b}$$

Besides the scattering angle, the two coefficients depend on the electron energy distribution.

Our strategy consists in modeling the scattering considering populations of electrons distributed according to angle dependent *effective* energy distributions. Our basic assumption is that the kernel of single scattering has the same form as given by equation (2.11), but photons are scattered in different directions by electrons with different energy distributions, so that their mean energy after the scattering is described by equation (2.28).

We define an effective angle dependent energy distribution $N_{\text{eff}}$ such as

$$\left[\int_1^\infty d\gamma(\gamma^2 - 1)N_{\text{eff}}(\gamma,\omega) + 1\right]\chi(\omega) = \left[\int_1^\infty d\gamma(\gamma^2 - 1)N(\gamma) + 1\right] \tag{2.30}$$

so that the averaged anisotropic kernel can be written as

$$\tilde{K}_P(x\omega\mathbf{u}, x'\mathbf{u}) = \phi(\omega)\int_0^\infty d\gamma\, K_P(x, x', \gamma)\, N_{\text{eff}}(\gamma,\omega) \ . \tag{2.31}$$

wher $\mathbf{u}$ is a unit vector parallel to the input photon direction.

Finally the anisotropic photon distribution after the scattering can be calculated from:

$$T_{k+1}(x\omega\mathbf{u}, z) \equiv T_{k+1}(x, \phi, \xi, z) = \int_0^\tau dz\, K_\nu(z, z') \int_0^\infty dx'\, K_p(x\omega\mathbf{u}, x'\mathbf{u})\, T_k(x'\mathbf{u}, z') \tag{2.32}$$

In the above calculations a beam of radiation scattered by an isotropic electron distribution has been assumed, considering the direction of the beam as reference axis. In the next Section 3.2 these results will be used to model the anisotropic scattering for a generic axisymmetric distribution of input photons, and the probability density distribution $T_{k+1}(x\Omega, z)$ will be computed relative to the symmetry axis of the input radiation distribution.

### 2.4.2 Anisotropic first scattering distribution

Herefater we consider a given axisymmetric distribution of photons $T_0(x\Omega, z)$ within a plane parallel scattering medium. In the assumed geometry the anisotropy of the radiation field is forced to produce relevant spectral distortions in the first scattering distribution only (see Section 3.4 and 4). In the present Section we consider only the evolution from $T_0(x\Omega, z)$ to $T_1(x\Omega, z)$, although the formalism developed in the previous Section 2.4.1 has a general validity.

In the following we indicate with $\mu'$ and $\mu$ the cosine of the angles between the reference axis (i.e. the normal at the slab) and the photon direction before and after the scattering, respectively.

As a first step, we compute the distribution $P(\omega, \mu, \mu')$ of the scattering angle in direction $\mu$ for a given initial direction $\mu'$. The problem can be solved by means of

simple geometrical arguments, noting that

$$\omega = \mu\mu' + \sqrt{1-\mu^2}\sqrt{1-\mu'^2}\cos(\rho-\rho') \ , \tag{2.33}$$

where $\rho'$ and $\rho$ define the azimuthal angle before and after the scattering, respectively. Due to symmetry, we can set $\rho' = 0$, and we find

$$d\rho = \pm(1-\mu^2-\mu'^2+2\mu\mu'\omega-\omega^2)^{-1/2}d\omega \ . \tag{2.34}$$

It is easy to see that

$$P(\omega,\mu,\mu') = 2\left|\frac{d\rho}{d\omega}\right| \tag{2.35}$$

where the factor 2 takes into account the change of sign in $d\rho$. Because of the symmetry of the problem, the distribution $P$ is independent on the azimuthal angle. Now we can compute the anisotropic averaged kernel as

$$K_{\mathcal{P}}(x\mu\mathbf{u},x'\mu'\mathbf{u}) \equiv \int_{\omega_1}^{\omega_2} d\omega\, K_{\mathcal{P}}(x\omega\mathbf{u},x'\mathbf{u})P(\omega,\mu,\mu') \tag{2.36.$a$}$$

Finally the first order distribution $T_1$ is

$$T_1(x\mu\mathbf{u},z) = \int_0^{\tau} dz'\, K_{\mathcal{V}}(z,z') \int_{-1}^{+1} d\mu'\, f(\mu',z') \int_0^{\infty} dx'\, K_{\mathcal{P}}(x\mu\mathbf{u},x'\mu'\mathbf{u})\, T_0(x'\mu'\mathbf{u},z') \tag{2.36.$b$}$$

where the two integration limits in $\omega$ read

$$\begin{aligned} \omega_1 &= \mu\mu' - \sqrt{1-\mu^2}\sqrt{1-\mu'^2} \\ \omega_2 &= \mu\mu' + \sqrt{1-\mu^2}\sqrt{1-\mu'^2} \ . \end{aligned} \tag{2.37}$$

Note that

$$\frac{1}{2\pi}\int_{\omega_1}^{\omega_2} d\omega P(\omega,\mu,\mu') = 1 \ . \tag{2.38}$$

The function $f(\mu',z')$ in eq.[2.36.b] takes into account that, since a plane parallel scattering medium has a *finite* vertical extension, photons travelling at grazing angles ($\mu' \sim 0$) have a mean scattering probability higher than photons travelling in the slab along the

normal ($\mu' \sim 1$). The angular distribution of the input photons must be weighted by means of the appropriate source function. Since the direct escape probability for input photon injected in $z'$ along direction $\mu'$ is $\propto \exp[(z' - \tau)/\mu']$, where $\tau$ is the optical depth of the slab calculated along the symmetry axis, we have

$$f(\mu', z') \equiv 1 - \exp[(z' - \tau)/\mu')] \tag{2.39}$$

Note that now $T_1$ must be normalized dividing eq.[2.36] by the factor

$$\int_0^\tau dz' \int_{-1}^{+1} d\mu' f(\mu', z') \int_0^\infty dx' T_0(x'\mu'\mathbf{u}, z') \tag{2.40}$$

The above procedure is valid only for the first order distribution $T_1(x\mu\mathbf{u}, z)$. Higher order scatterings can be treated as in the case of complete isotropy. An average isotropic distribution can be used to compute $T_2(x, z)$.

A simplified calculation consists in considering the averaged coefficients $\phi(\mu, \mu')$ and $\xi(\mu, \mu')$ given by

$$\phi(\mu, \mu') = \frac{1}{2\pi} \int_{\omega_1}^{\omega_2} d\omega P(\omega, \mu, \mu')\phi(\omega) \tag{2.41.a}$$

and

$$\xi(\mu, \mu') = \frac{1}{2\pi} \int_{\omega_1}^{\omega_2} d\omega P(\omega, \mu, \mu')\xi(\omega) \ . \tag{2.41.b}$$

Note that the correct value of $\chi$ defined as $\xi(\mu, \mu')/\phi(\mu, \mu')$, and not as a mean value computed via equation (2.41.a) or equation (2.41.b). The anisotropic distribution $T_1$ is then computed as

$$T_1(x\mu\mathbf{u}, z) = \int_0^\tau dz' \, K_\mathcal{V}(z, z') \int_{-1}^{+1} d\mu' \, f(\mu', z') \int_0^\infty dx' \, K_\mathcal{P}(x\mu\mathbf{u}, x'\mu'\mathbf{u}) \, T_0(x'\mu'\mathbf{u}, z') \tag{2.42}$$

where the averaged kernel is constructed with the averaged anisotropy coefficeints defined above.

The approximated formulation given above is particularly convenient since the integrals in equation (2.41.a) and (2.41.b) can be explicitly solved using for $\phi(\omega)$ and

$\xi(\omega)$ a polynomial approximation of arbitrary order. The calculation is described in Section 2.5 for the case of thermal Comptonization.

Finally it is important to note that the calculation developed in the last section are greatly simplified (see Haardt 1993) if the input distribution $T_0(x\mu\mathbf{u}, z)$ has the form $X_0(x)U_0(\mu)$.

## 2.5 THE THERMAL CASE

### 2.5.1 Effective electron distribution

We specialize our treatment for a thermal electron distribution. The electron energy distribution is in this case

$$N(\gamma) = \frac{1}{\Theta \mathrm{K}_2(1/\Theta)} \gamma(\gamma^2-1)^{1/2} \mathrm{e}^{-\gamma/\Theta} \ , \tag{2.43}$$

where $\mathrm{K}_2$ is the second order modified Bessel function.

It is easy to see that the total number of electrons is normalized so as

$$\int_1^\infty d\gamma N(\gamma) = 1 \ , \tag{2.44}$$

while the fractional mean energy gain per scattering suffered by photons is proportional to

$$\int_1^\infty d\gamma(\gamma^2-1)N(\gamma) = \frac{12\Theta^2\mathrm{K}_2(1/\Theta) + 3\Theta\mathrm{K}_1(1/\Theta)}{2\Theta\mathrm{K}_1(1/\Theta) + \mathrm{K}_0(1/\Theta)} \ . \tag{2.41}$$

Using definition (2.30) we can define an (angle dependent) *effective* temperature $\tilde{\Theta}(\omega, \Theta)$ for the scattering as solution of the following equation:

$$\left[\frac{16\Theta^2\mathrm{K}_2(1/\Theta) + 4\Theta\mathrm{K}_1(1/\Theta)}{2\Theta\mathrm{K}_1(1/\Theta) + \mathrm{K}_0(1/\Theta)} + 1\right] \chi(\omega) = \frac{16\tilde{\Theta}^2\mathrm{K}_2(1/\tilde{\Theta}) + 4\tilde{\Theta}\mathrm{K}_1(1/\tilde{\Theta})}{2\tilde{\Theta}\mathrm{K}_1(1/\tilde{\Theta}) + \mathrm{K}_0(1/\tilde{\Theta})} + 1 \ . \tag{2.42}$$

and then an (angle dependent) *effective* number density

$$N_{\mathrm{eff}}(\gamma, \omega) = \frac{1}{\tilde{\Theta}\mathrm{K}_2(1/\tilde{\Theta})} \gamma(\gamma^2-1)^{1/2} \mathrm{e}^{-\gamma/\tilde{\Theta}} \tag{2.43}$$

The averaged anisotropic kernel is then computed via eq.[2.31].

### 2.5.2 Polynomial Approximations

The computational method previously described needs a tractable form for $\phi(\omega)$ and $\xi(\omega)$. We recall that the two coefficients are functions of the electron temperature, besides the scattering angle. The most convenient procedure is to find polynomial approximations for $\phi(\omega)$ and $\xi(\omega)$. We note that for high $\Theta$ and $\omega \simeq 1$ the anisotropy coefficients tend to be $\sim 0$ (see below), and the ratio of the two polynomials could diverge when both the coefficients are small. It is then convenient to find an anlytical approximation for $\chi(\omega)$, writing $\xi(\omega)$ as $\chi(\omega)\phi(\omega)$.

We have performed a Montecarlo simulation of single scattering for a beam of monoenergetic radiation, computing $\phi(\omega)$ and $\chi(\omega)$ in 20 angular bins with width $\Delta\omega = 0.1$, for eight different values of $\Theta$ (0.05, 0.1, 0.25, 0.5, 0.75, 1., 3., 5.). Then we have performed a 2-dimensional fitting to simulations by means of third order polynomials in $\omega$:

$$\phi(\omega) = \sum_{\mathrm{i}=0}^{3} Q_{\mathrm{i}}(\Theta)\omega^i \tag{2.44}$$

and

$$\chi(\omega) = \sum_{\mathrm{i}=0}^{3} R_{\mathrm{i}}(\Theta)\omega^i \ . \tag{2.45}$$

From $\xi = \phi\chi$, using the above expressions we find

$$\xi(\omega) = \sum_{\mathrm{i}=0}^{6} Z_{\mathrm{i}}(\Theta)\omega^i \tag{2.46}$$

where the coefficients $Z$ can be expressed as combinations of $Q$ and $R$.

From equation (2.29.a) and (2.29.b) we have a constrain for $Q_0$ and $Z_0$:

$$Q_0 = 1 - \frac{Q_2}{3} \tag{2.47.a}$$

and

$$Z_0 = 1 - \frac{Z_6}{7} - \frac{Z_4}{5} - \frac{Z_2}{3} \ . \qquad (2.47.b)$$

By definition (eq. [2.27]), in the limit of low temperature, $\phi(\omega)$ coincides with the Ryleigh phase function times $4\pi$, while (eq.[2.28]) $\chi(\omega)$ is $\simeq 1$. A further constrain is due to the fact that for high temperatures the effects of anisotropy do saturate (Ghisellini et al. 1991) Then we write the $Q$s in the following suitable form:

$$\begin{aligned} Q_3(\Theta) &= \frac{c_{32}\Theta^2 + c_{31}\Theta}{16\Theta^2 + 4\Theta + 1} \\ Q_2(\Theta) &= \frac{c_{22}\Theta^2 + c_{21}\Theta + 3/4}{16\Theta^2 + 4\Theta + 1} \\ Q_1(\Theta) &= \frac{c_{12}\Theta^2 + c_{11}\Theta}{16\Theta^2 + 4\Theta + 1} \end{aligned} \qquad (2.48.a)$$

and the $R$s as

$$\begin{aligned} R_3(\Theta) &= \frac{c_{32}\Theta^2 + c_{31}\Theta}{16\Theta^2 + 4\Theta + 1} \\ R_2(\Theta) &= \frac{c_{22}\Theta^2 + c_{21}\Theta}{16\Theta^2 + 4\Theta + 1} \\ R_1(\Theta) &= \frac{c_{12}\Theta^2 + c_{11}\Theta}{16\Theta^2 + 4\Theta + 1} \ . \end{aligned} \qquad (2.48.b)$$

The best fit values of the numerical coefficients $c$ relative to the $\phi$ and $\chi$ fitting are reported in Table 1.

In Fig. 1 the polynomial approximation is compared with numerical results. The fits are sufficiently good for our purposes.

In practical computation is conveninet to use the mean values defined in equation (2.41.a) and (2.41.b). We remind that the proper value of $\chi(\mu, \mu')$ should be computed as $\xi(\mu, \mu')/\phi(\mu, \mu')$. The integrations in equation (2.41.a) and (2.41.b) are cumbersome but not difficult. The solution of integral (2.41.b) can be written as

$$\xi(\mu, \mu') = \sum_{i=0}^{6} h_i(\mu, \mu') Z_i \qquad (2.49.a)$$

**TABLE 1**

Best Fit Coefficients of Polynomial Approximations

| | $\phi(\omega)$ | $\chi(\omega)$ |
|---|---|---|
| $c_{32}$ | 0.034 | 1.108 |
| $c_{31}$ | 0.580 | 0.184 |
| $c_{22}$ | -0.367 | -0.023 |
| $c_{21}$ | 0.144 | 1.121 |
| $c_{12}$ | -16.000 | -12.927 |
| $c_{11}$ | 0.803 | -5.149 |

where

$$h_0 = 1$$

$$h_1 = \mu\mu'$$

$$h_2 = \frac{1}{2}(1 - \mu^2 - \mu'^2 + 3\mu^2\mu'^2)$$

$$h_3 = \frac{1}{2}\mu\mu'(3 - 3\mu^2 - 3\mu'^2 + 5\mu^2\mu'^2)$$

$$h_4 = \frac{1}{8}(3 - 6\mu^2 + 3\mu^4 - 6\mu'^2 + 36\mu^2\mu'^2 - 30\mu^4\mu'^2 + 3\mu'^4 - 30\mu^2\mu'^4 + 35\mu^4\mu'^4)$$

$$h_5 = \frac{1}{8}\mu\mu'(15 - 30\mu^2 + 15\mu^4 - 30\mu'^2 + 100\mu^2\mu'^2 - \\ - 70\mu^4\mu'^2 + 15\mu'^4 - 70\mu^2\mu'^4 + 63\mu^4\mu'^4)$$

$$h_6 = \frac{1}{16}(5 - 15\mu^2 + 15\mu^4 - 5\mu^6 - 15\mu'^2 + 135\mu^2\mu'^2 - 225\mu^4\mu'^2 + 105\mu^6\mu'^2 + 15\mu'^4 - \\ - 225\mu^2\mu'^4 + 525\mu^4\mu'^4 - 315\mu^6\mu'^4 - 5\mu'^6 + 105\mu^2\mu'^6 - 315\mu^4\mu'^6 + 231\mu^6\mu'^6) \quad (2.49.b)$$

Note that the above expression is symmetric in $\mu$ and $\mu'$, and that the integral over the total solid angle is equal 1. The integral in equation (2.41.a) is analogous, reading

$$\phi(\mu, \mu') = \sum_{i=0}^{3} h_i(\mu, \mu') Q_i \quad (2.50)$$

### 2.5.3 Examples of thermal IC spectra

The computational method developed in the previous Section can be used to calculate angle-dependent IC spectra. Here we briefly describe the calculation procedure, assuming Thomson scattering in a plane parallel geometry. Every model is computed for given values of the input parameters, namely $\Theta$, $\tau$ and $\mu$. An initial condition $T_0(x\mu\mathbf{u}) = X_0(x)U_0(\mu)\delta(z-0)$ is considered. where $X_0$ is the Planck law, and $U_0$ is a limb darkening law (Chandrasekhar 1960).

The probabilities $p_k$ can be computed a priori using the formalism described in §2.2.2 for the case of Thomson scattering. The heart of the code is the computation of $X_k$ from $X_{k-1}$. We sample $X_k$ on the x-axis in n different points such as $x_{k,j} = c \times x_{k-1,j}$. The factor $c$ does not depend on k, and choosing $c \sim 16\Theta^2 + 4\Theta + 1$, the 1-D grid is roughly centered on the considered $X_k$. If we use a logarithmic grid, $2n-1$ values of $\epsilon = x_{k,h}/x_{k-1,i}$ are possible:

$$\epsilon_j = \frac{x_{k,1}}{x_{k-1,j}} \quad j = 1,n$$

$$\epsilon_{n+j-1} = \frac{x_{k,j}}{x_{k-1,1}} \quad j = 2,n$$

It is important to note that the possible values expressed by the last formula do not depend on the particular order of scattering, i.e. the kernel $G$ (eq.(6)) is independent from k. This allows us to compute a priori a set of $2n-1$ values of the kernel $G$ defined by eq.(6). Integral (4) can be solved by means of a simple linear extrapolation of $X_{k-1}G$ between sampling points where the values of $G$ do not change with k. The integration limits in eq.(4) depends on the energy where $X_k$ is evaluated. For example in order to compute $X_k$ in the first sampling energy $x_{k,1}$, the integration must be performed from $x_{k-1,1}$ to $x_{k-1,n}$, for the second energy $x_{k,2}$ from $x_{k-1,2}$ to $x_{k-1,n+1}$, and so on, till the last sampling energy $x_{k,n}$ from $x_{k-1,n}$ to $x_{k-1,2n-1}$.

The same algorithm is adequate to compute the first anisotropic distribution $\tilde{S}_1$. We select m values of $\mu'$, and we calculate m values of $\phi(\mu,\mu')$ and $\xi(\mu,\mu')$ as previously discussed. Using the procedure described above we can find a set of m $\tilde{S}_1(x,\mu,\mu')$ distributions, and by means of a linear extrapolation between the angular sampling

points, the integral (25) can be solved. Note that an isotropic distribution $X_1$ can be used to compute $X_2$. If the same model for a different viewing angle is needed, one can re-calculate only $\tilde{S}_1$ (and the probabilities $p_k$), since the successive distributions $S_2$, $S_3$ and so on, are independent on $\mu$.

In figures from 2.a,b,c to 6.a,b,c some examples of calculation are shown. We have plotted the photon flux (defined as $xf(x)$) in order to compare results with the output of Montecarlo simulations. As can be seen the agreement is sufficiently good for a wide range of input parameters. As discussed in the previous Section, the errors due to the approximated treatment of $f_1$ are more evident for high inclination angles. From figure ? it can be seen how the flux relative to $f_1$ is slightly overestimates for grazing angles.

The IC spectrum is formed by the sum of the single scattering spectra, each of them reflecting in shape (in some way) the energy distribution of the electrons. In the case of thermal electrons the total spectrum can be approximated by a power law $f \propto x^{-\alpha-1}$ if the temperature is sufficiently low and the opacity high so that single spectra are closely "packaged" in the frequency axis. Power law shape occurs up to energies for which the electron recoil is negligible. The power law approximation is not tenable when the electron temperature is high and the opacity low. In this case features of single spectra are clearly visible (see figures ?).

In general the spectral index $\alpha$ depends on $\tau$ and $\Theta$. If the Compton emission from a slab is integrated over all directions, for $\tau < 1$ and $\Theta > 0.1$, good agreements with numerical simulations are obtained with

$$\alpha = [-\ln(\tau) + 2/(3+\Theta)]/[\ln(12\Theta^2 + 25\Theta)] \tag{2.51}$$

Taking into account the angular dependency of the radiated photons, the main feature found with our calculations is the deficiency of power in the first scattering distribution for low inclination angles. This fact causes evident spectral distortions. In the region dominated by $f_1$, the spectrum is considerably flatter than the average one. We have

empirically found that a broken power law can qualitatively fit the spectrum. Defining $A_1$ as the mean energy gain per scattering, for $\chi_1 A_1 < x < A_1^3$ the spectral index is given by:

$$\tilde{\alpha} = [-\ln(\tau/\phi_1) + 2/(3+\Theta)]/\ln[(12\Theta^2 + 25\Theta)/\chi_1] \tag{2.52}$$

while for $x > A_1^3$ good fit are obtained with the average formula (41). In general for $\mu > 0$ $\tilde{\alpha}$ is lower than $\alpha$, viceversa for $\mu < 0$. The flatter spectra are seen at low inclination angles.

## REFERENCES

Chandrasekhar S., 1960, Radiative Transfer. Dover, New York

Coppi P. S., Blandford R. D., 1990, MNRAS, 245, 453

Gautschi W., & Cahill W. F., 1970, in Handbook of Mathematical Functions: nineth edition, ed. by M. Abramowitz and I. A. Stegun, Dover, New York, p.227

Ghisellini G., George I. M., Fabian A. C., Done C., 1991, MNRAS, 248, 14

Haardt F., 1993, ApJ, 413, 680

Jones F. C., 1968, Phys.Rev., 167, 1159

Nishimura J., Mitsuda K., Itoh M., 1986, PASJ, 38, 819

Pozdnyakov L. A., Sobol' I. M., Sunyaev R. A., 1983, Ap. Space Sc. Rev., Vol. 2, p. 189

Rybicki G. B., Lightman A. P., 1979, Radiative Processes in Astrophysics, Wiley, New York

Sunyaev R. A., Titarchuk L. G., 1980, A&A, 86, 121

## FIGURE CAPTIONS

**Figure 1:** Montecarlo calculations and polynomial approximations of the anisotropy coefficients $\phi(\omega)$ and $\chi(\omega)$ vs. the cosine of the scattering angle $\omega$. From top to the bottom the electron temperature is $\Theta = 0.05$, $\Theta = 0.5$ and $\Theta = 5$, respectively. Open squares refer to $\phi$, filled squares to $\chi$, as computed via numerical simulations. The polynomial approximations discussed in Section 3.3 are shown as continuous lines.

**Figure 2:** Computed IC spectrum compared with Montecarlo simulations. The total spectrum (solid line) is shown together with the single scattering ones (dashed lines). The step function shows the result of numerical simulations. The soft photon input is a black-body, with emissivity according to a limb darkening law with $b = 2$ (see eq. [39]). The input values of the parameters of the hot plasma are $\Theta = 1.7$ and $\tau = 0.15$, which yield a Compton parameter $y \simeq 8$. The cosine of the viewing angle is $\mu = 0.9$ for panel a, $\mu = 0.5$ for panel b, and $\mu = 0.1$ for panel c. Montecarlo spectra are averaged in cosine intervals of width $\Delta\mu = 0.2$ around the labelled value of $\mu$. The photon energy is in unit of $kT_{\rm bb}$ where $T_{\rm bb}$ is the black-body temperature. The low energy cut-off of $f_3$ and the anomalous behaviour of the first two energy bins of the simulated spectra are due to numerical approximations.

**Figure 3:** As Figure 2, but $\Theta = 1.59$ and $\tau = 0.01$. The resulting Compton parameter is $y \simeq 0.5$.

**Figure 4:** As Figure 2, but $\Theta = 0.188$ and $\tau = 0.06$. The resulting Compton parameter is $y \simeq 0.08$.

**Figure 5:** Analytical IC spectrum for $\Theta = 0.5$ and $\tau = 0.1$. Solid line refers to $\mu = 1$, dashed line to $\mu = 0.5$, dash-dotted line to $\mu = 0.1$ and long-short dashed line to $\mu = -0.5$.

**Figure 6:** As Figure 5, but $\Theta = 1$ and $\tau = 0.1$.

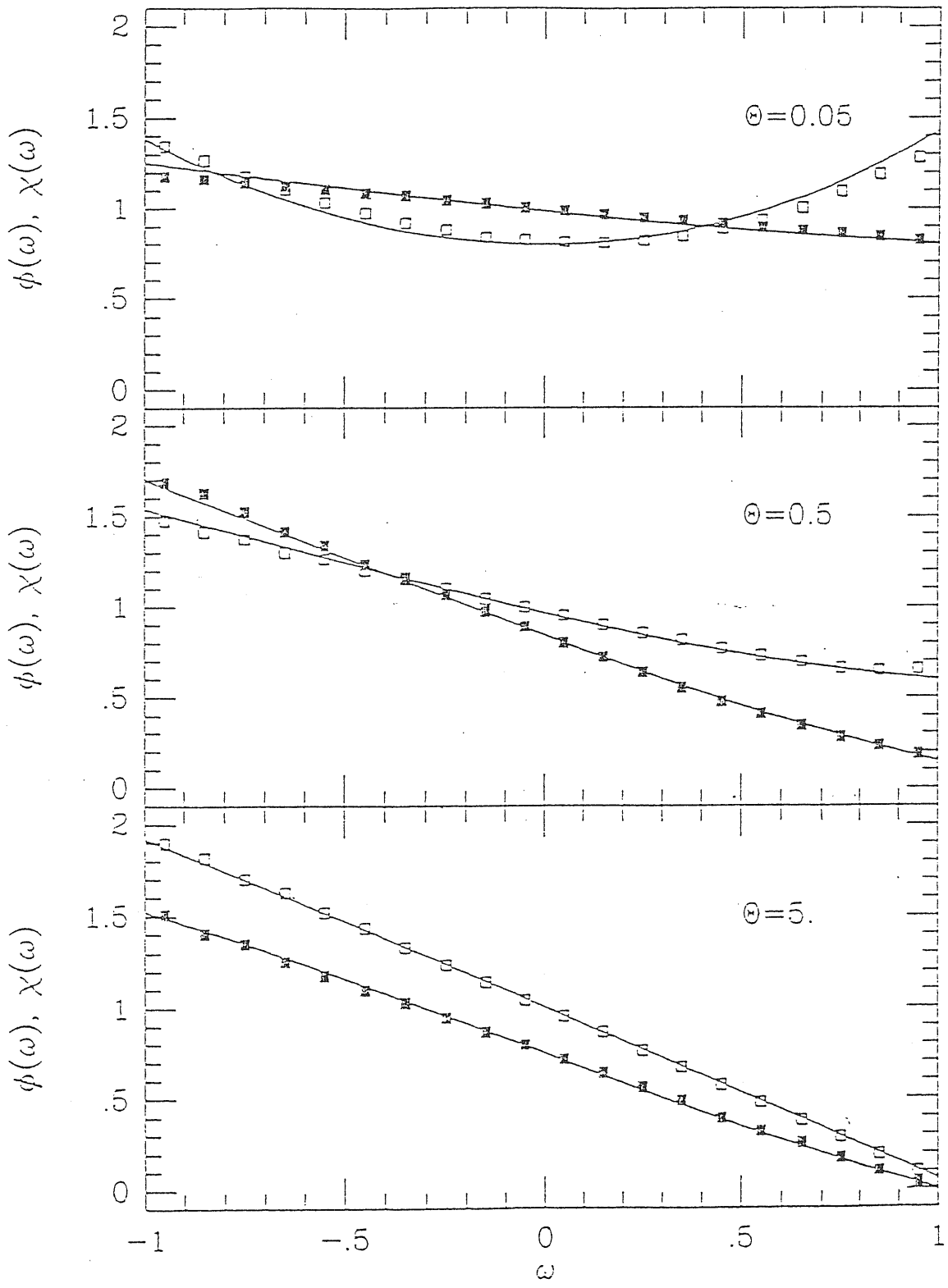
Θ=0.05
Θ=0.5
Θ=5.
φ(ω), χ(ω)
φ(ω), χ(ω)
φ(ω), χ(ω)
2
1.5
1
.5
0
−1
−.5
0
.5
1
ω

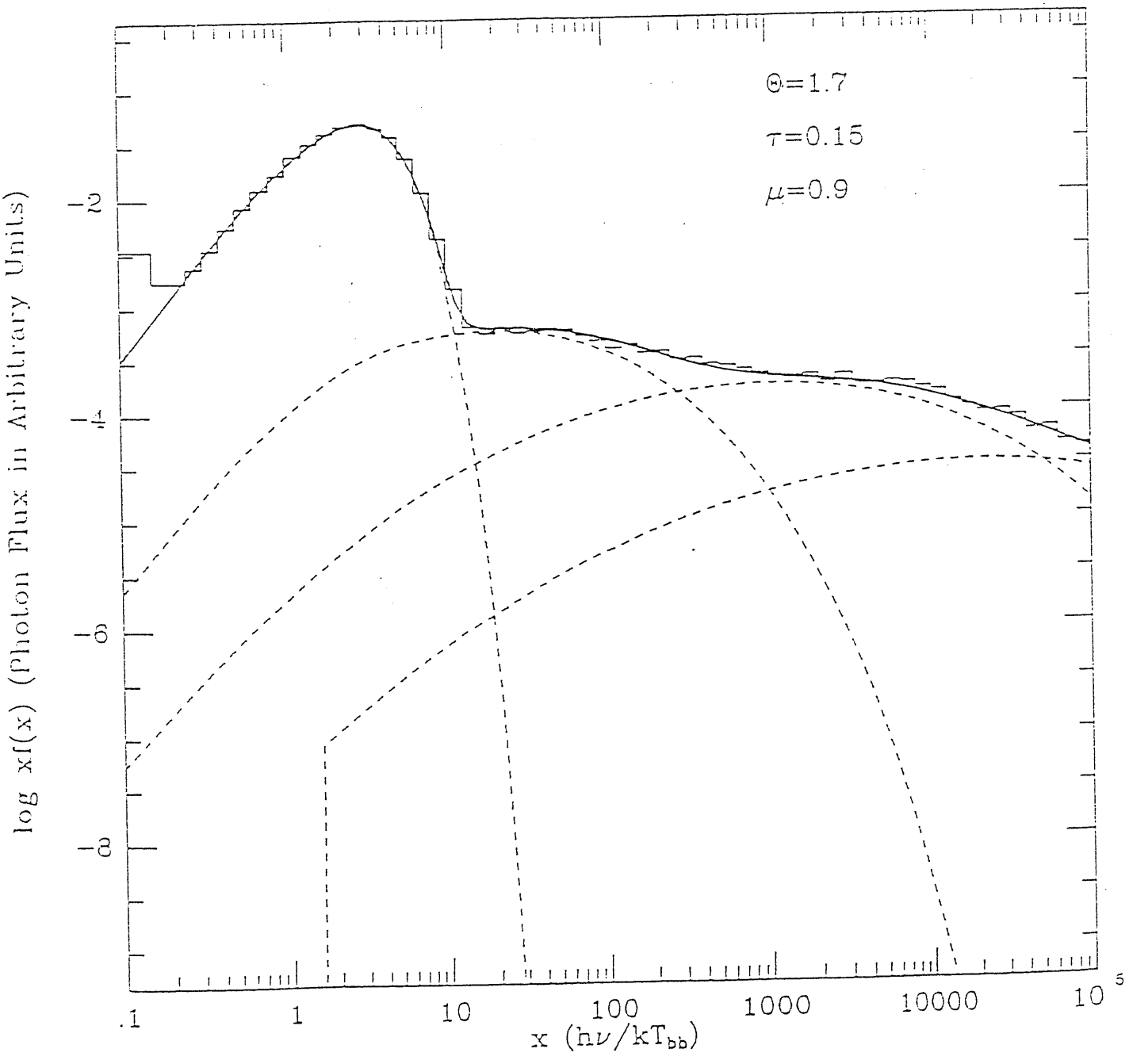
Θ=1.7
τ=0.15
μ=0.9
log xf(x) (Photon Flux in Arbitrary Units)
-2
-4
-6
-8
.1
1
10
100
1000
10000
10^5
x (hν/kT_bb)

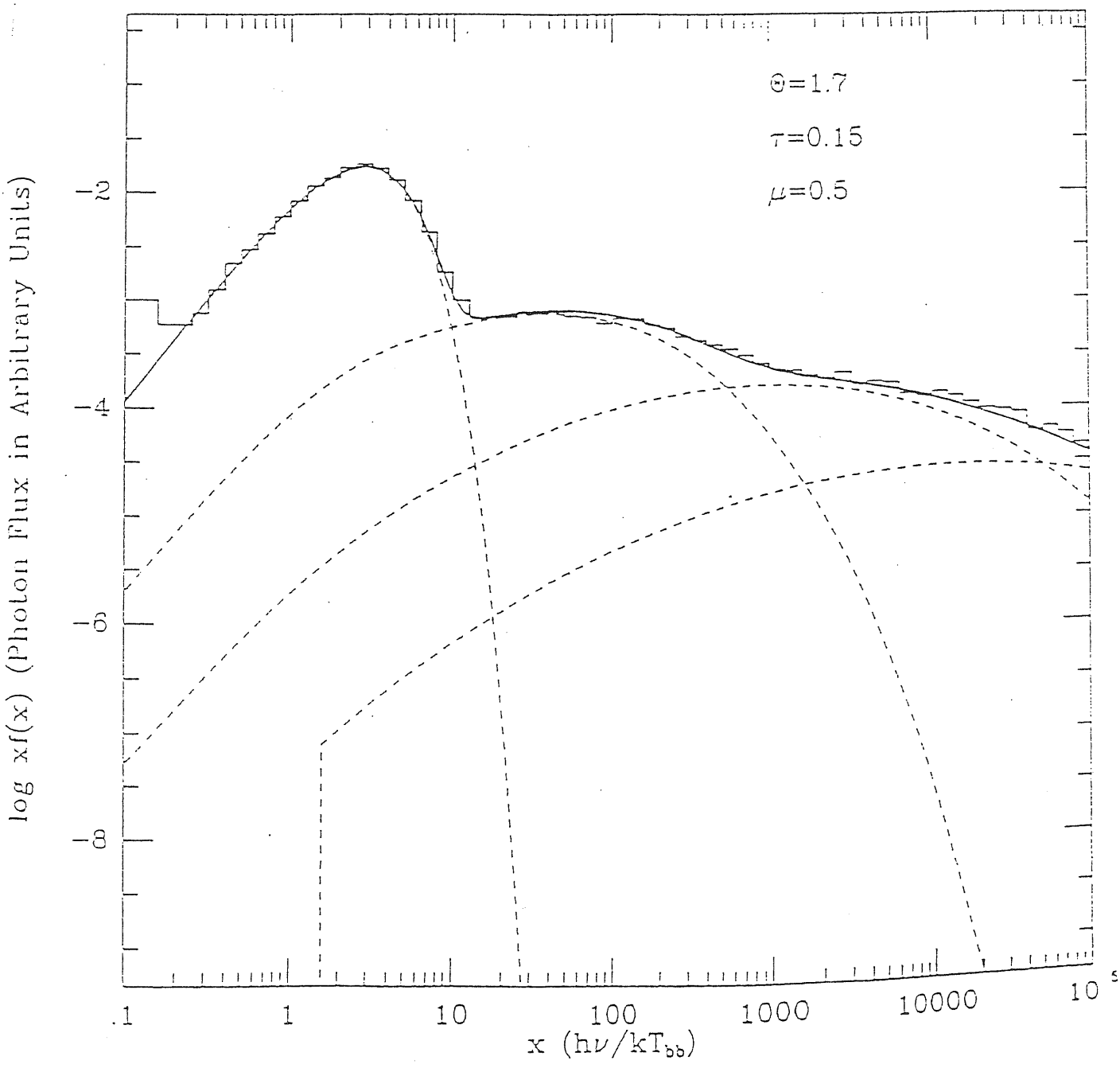
Θ=1.7
τ=0.15
μ=0.5
log xf(x) (Photon Flux in Arbitrary Units)
-2
-4
-6
-8
.1
1
10
100
1000
10000
x (hν/kT_bb)

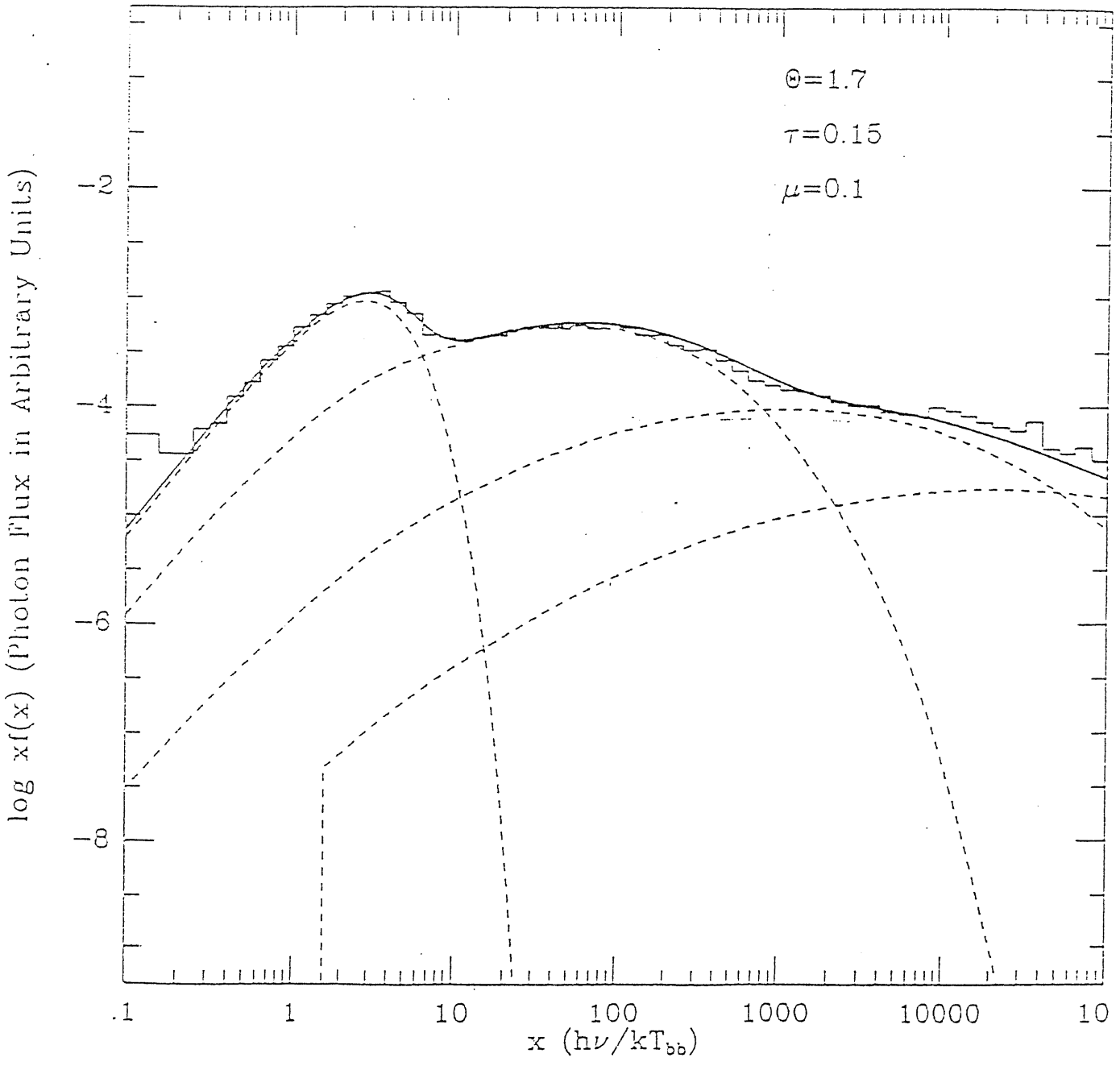
Θ=1.7
τ=0.15
μ=0.1
log xf(x) (Photon Flux in Arbitrary Units)
-2
-4
-6
-8
.1
1
10
100
1000
10000
x (hν/kT_bb)

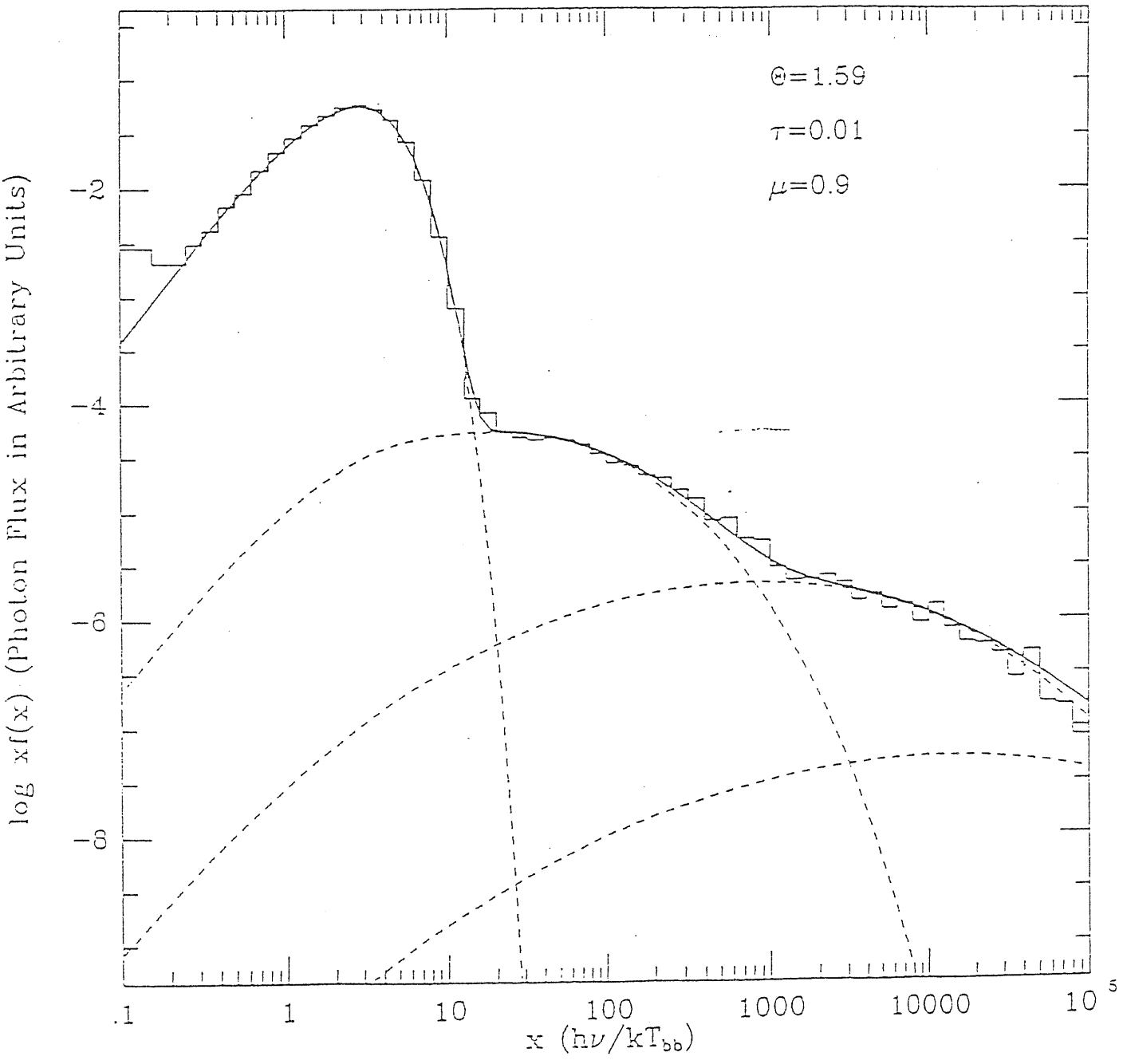
Θ=1.59
τ=0.01
μ=0.9
log xf(x) (Photon Flux in Arbitrary Units)
-2
-4
-6
-8
.1
1
10
100
1000
10000
10^5
x (hν/kT_bb)

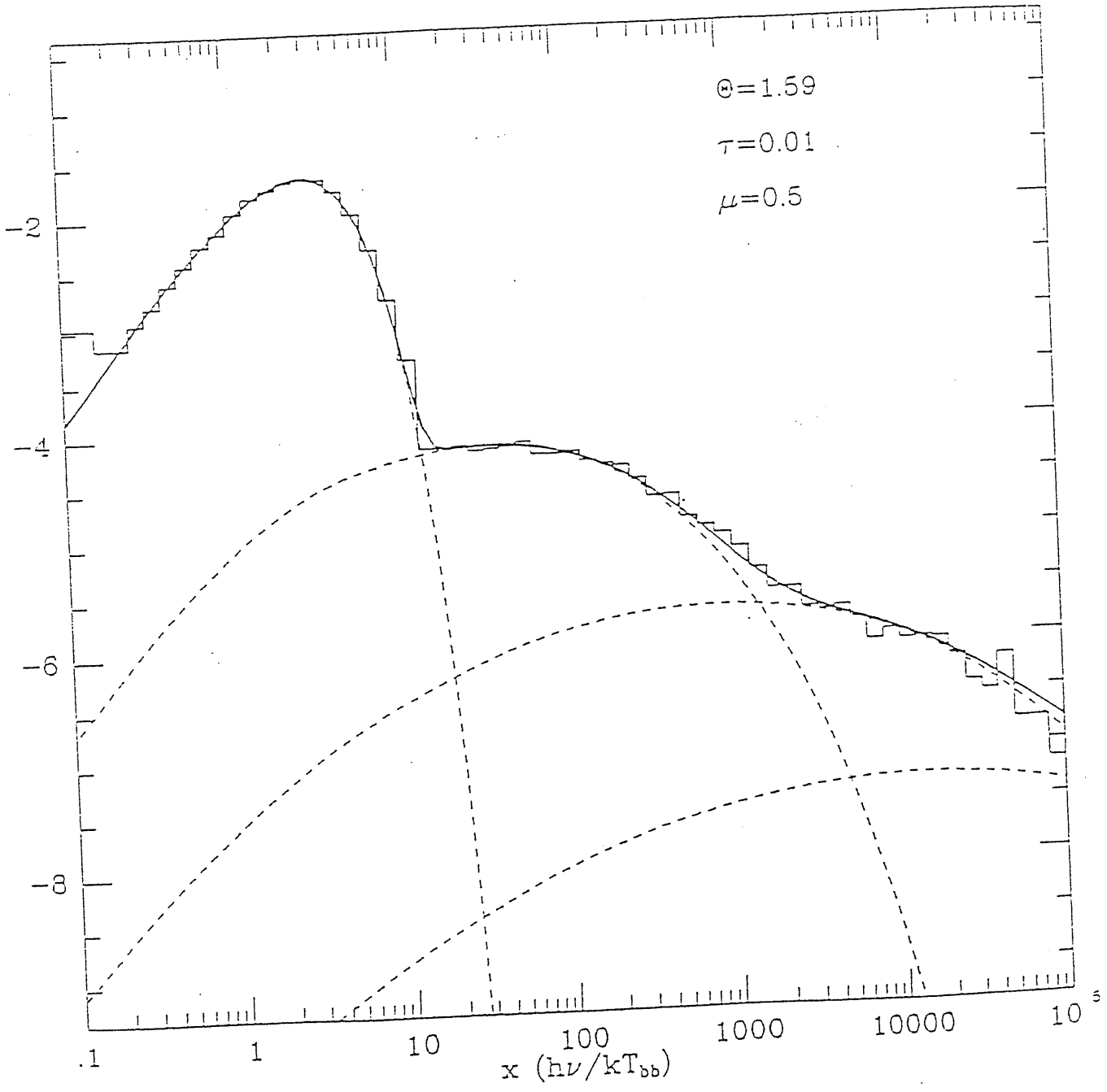
Θ=1.59
τ=0.01
μ=0.5
-2
-4
-6
-8
.1
1
10
100
1000
10000
10^5
x (hν/kT_bb)

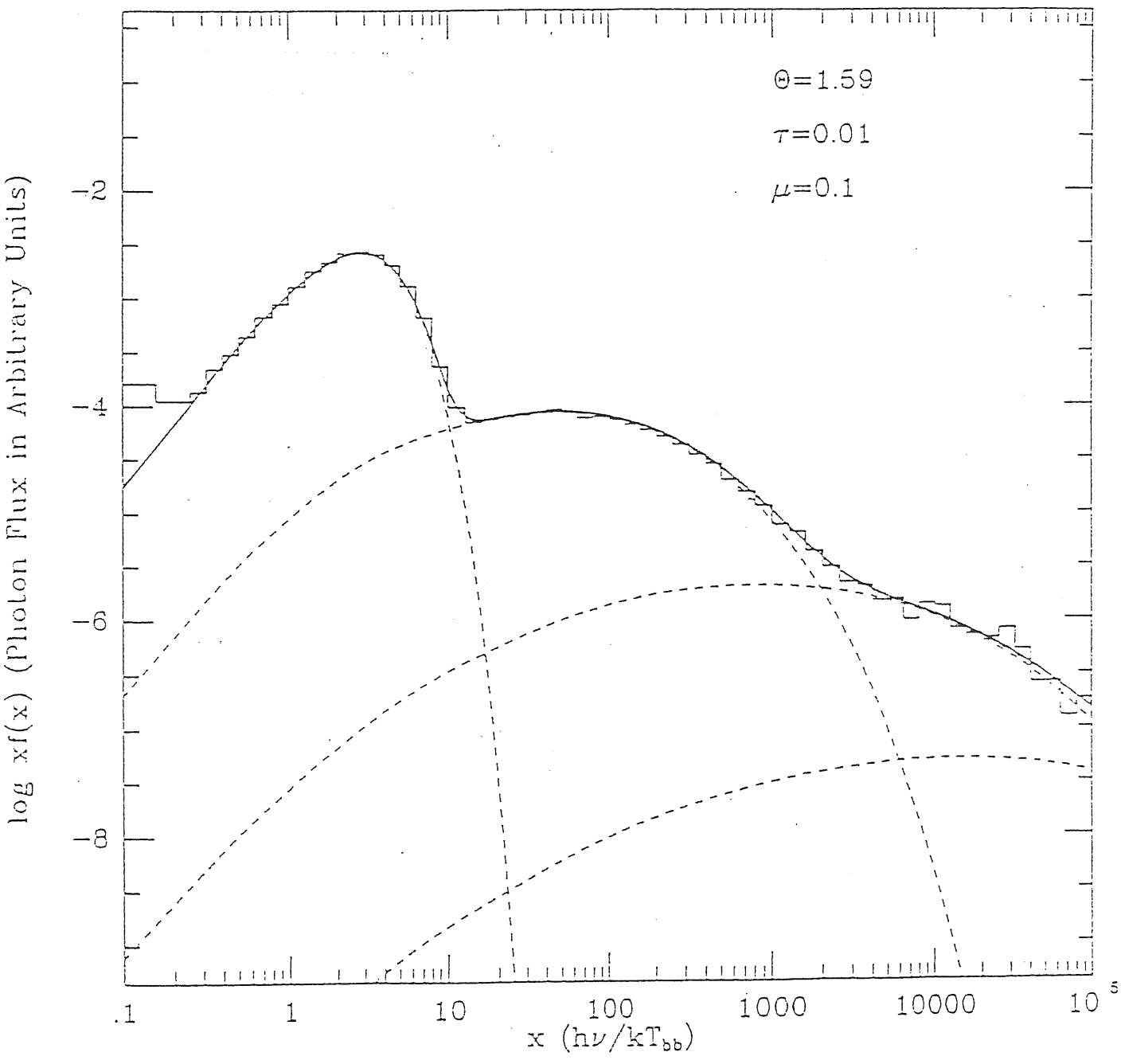
Θ=1.59
τ=0.01
μ=0.1
log xf(x) (Photon Flux in Arbitrary Units)
-2
-4
-6
-8
.1
1
10
100
1000
10000
10^5
x (hν/kT_bb)

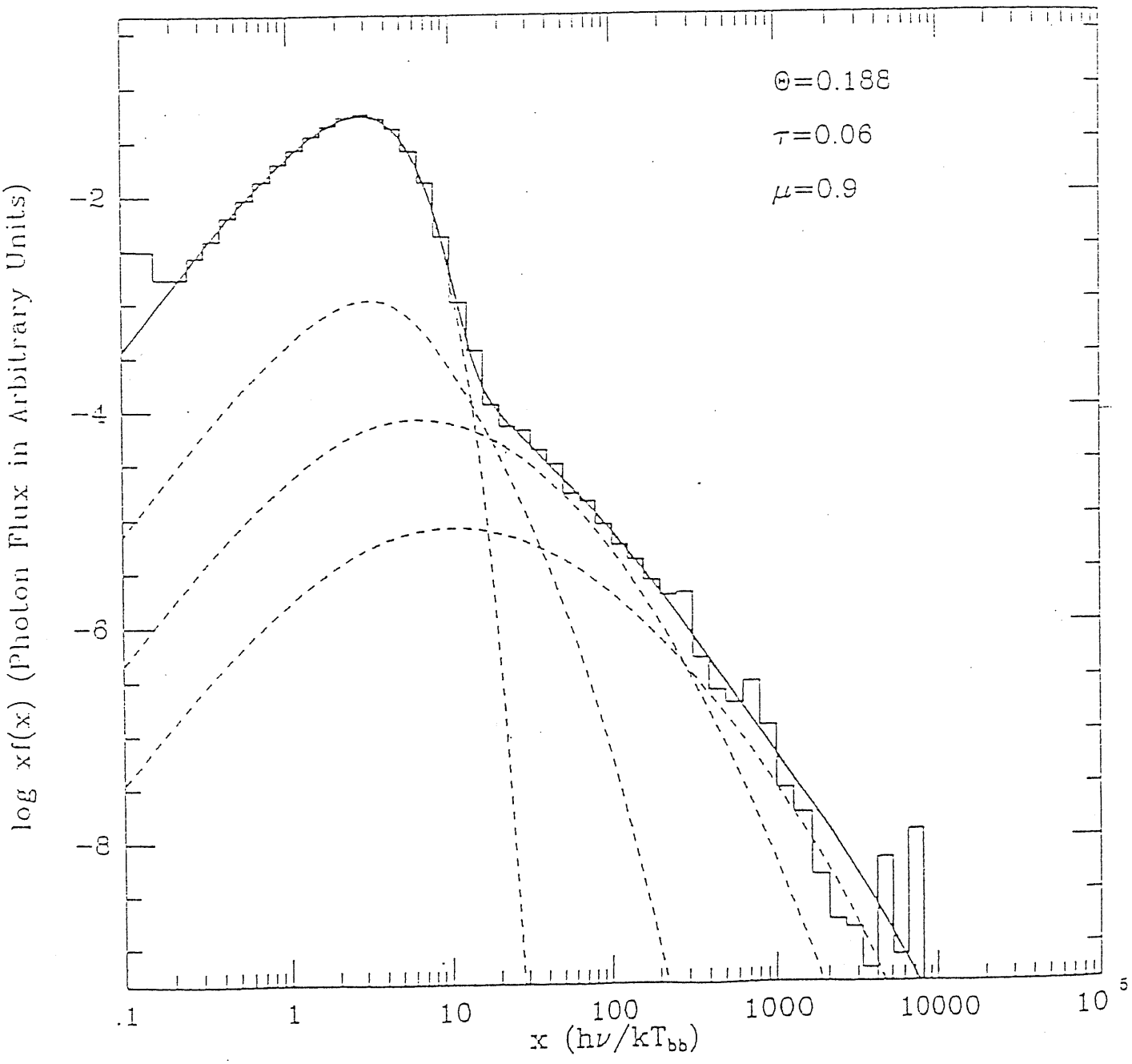
Θ=0.188
τ=0.06
μ=0.9
log xf(x) (Photon Flux in Arbitrary Units)
x (hν/kT_bb)
.1
1
10
100
1000
10000
10^5

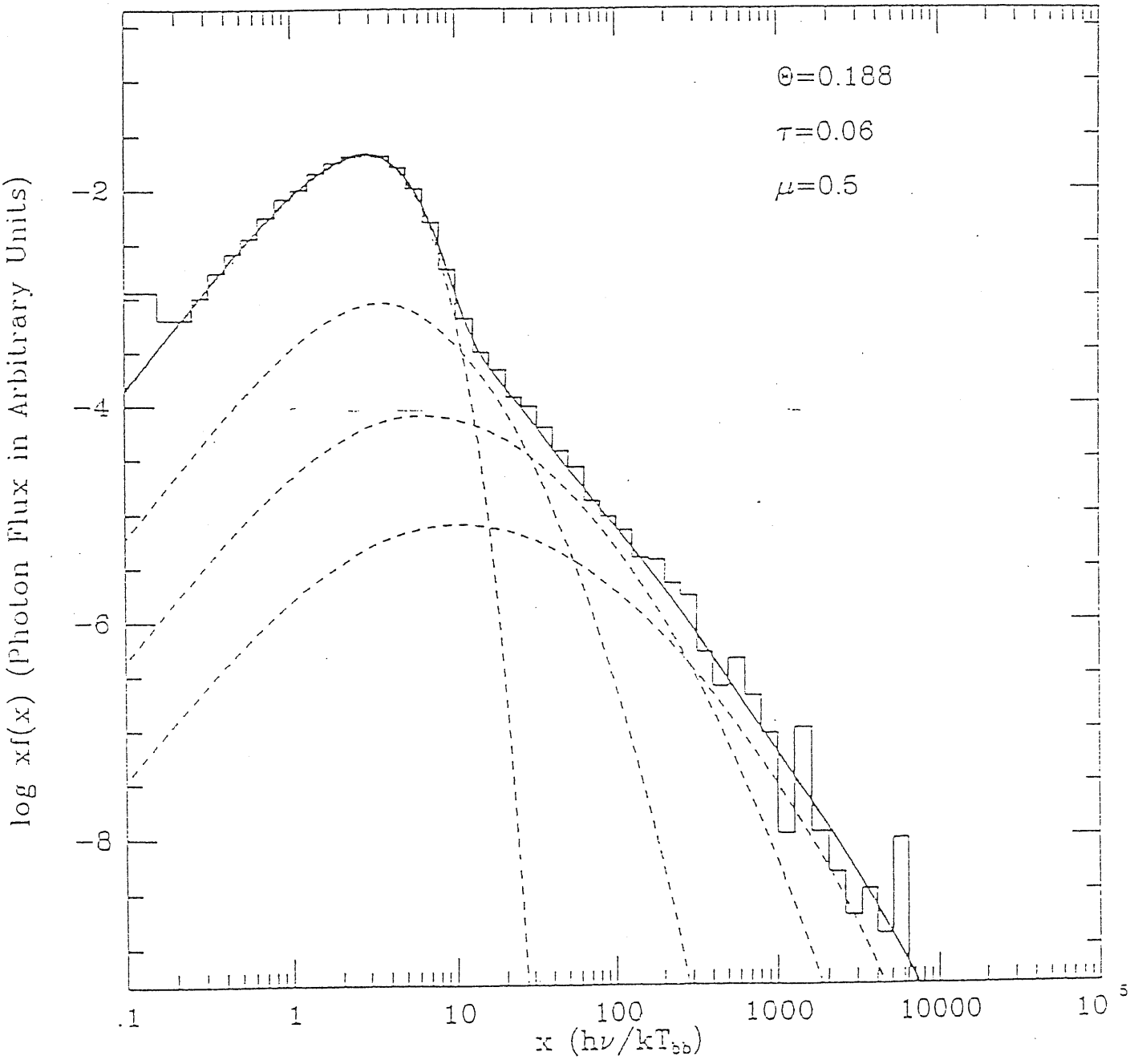
Θ=0.188
τ=0.06
μ=0.5
log xf(x) (Photon Flux in Arbitrary Units)
-2
-4
-6
-8
.1
1
10
100
1000
10000
10^5
x (hν/kT_bb)

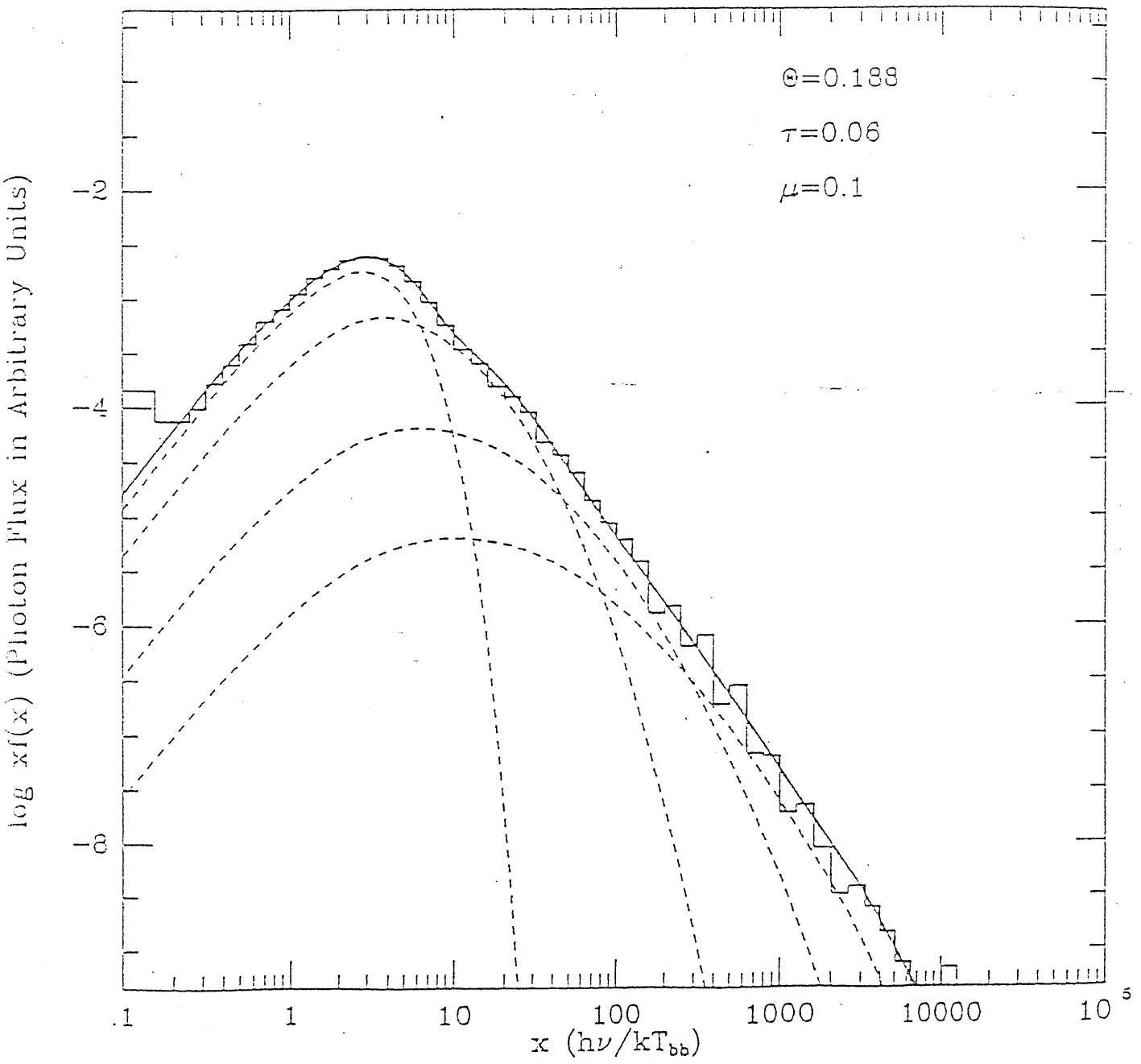
Θ=0.188
τ=0.06
μ=0.1
log xf(x) (Photon Flux in Arbitrary Units)
-2
-4
-6
-8
.1
1
10
100
1000
10000
10^5
x (hν/kT_bb)

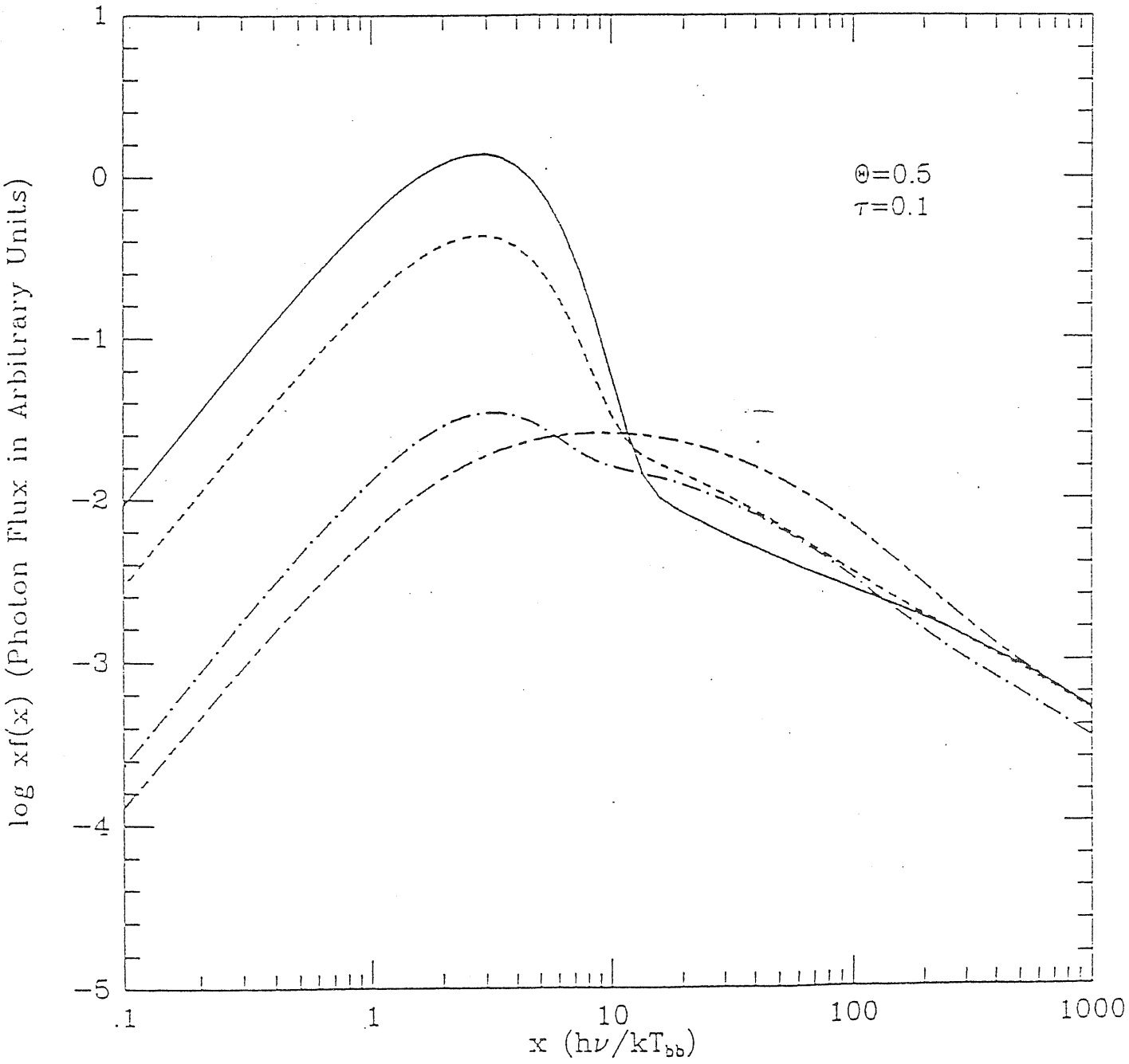
1
0
−1
−2
−3
−4
−5
.1
1
10
100
1000
log xf(x) (Photon Flux in Arbitrary Units)
x (hν/kT_bb)
Θ=0.5
τ=0.1

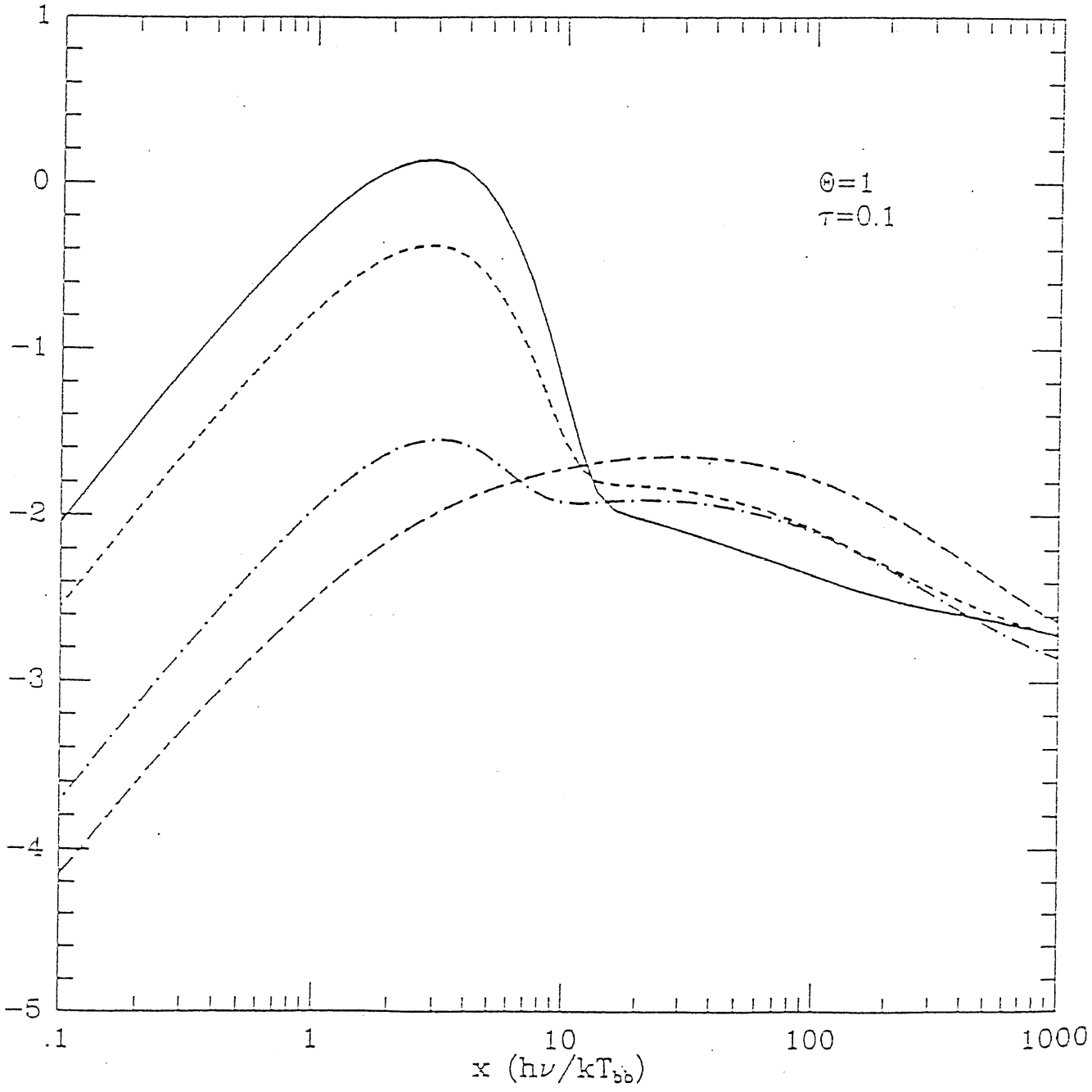
1
0
−1
−2
−3
−4
−5
.1
1
10
100
1000
x (hν/kT_bb)
Θ=1
τ=0.1